# 21 Concept of Mismatch and Relaxation for Self-Diffusion and Conduction in Ionic Materials with Disordered Structures

Klaus Funke, Cornelia Cramer, and Dirk Wilmer

## 21.1 Introduction

In the ion conducting materials to be discussed in this chapter, structural and dynamic disorder is the key property. A simple scheme may serve to highlight the remarkable implications of this property with regard to the movements of the ions. In this scheme, perfectly ordered crystals are placed at *level one*. At this level, there is no possibility for the ions to leave their sites; thus no ionic transport can occur. Historically, the decisive step forward was made when site disorder was discovered and point-defect thermodynamics were developed. At this stage, which we call *level two*, ionic transport is accomplished by point defects moving randomly from site to site. In fact, modern materials science and engineering build on the concept of level two.

Dramatic changes are encountered as we move on to materials with disordered structures, i.e., from level two to *level three*. Now, point defects are no longer isolated structural elements. It is even no longer sensible to *speak* of defects, since the entire structure is disordered. Therefore, ionic transport cannot be described in terms of individual defects performing random walks in a static energy landscape. Instead, we are facing a challengingly complicated many-particle problem, with the mobile ions interacting with each other and with their surrounding matrix.

In materials with disordered structures, the number of available sites by far exceeds the number of mobile ions, and it turns out to be impossible to arrange the ions unambiguously in an optimised manner. These materials may be crystalline or glassy. They are fast ion conductors, if the barrier to be surmounted in a hop is of the order of the thermal energy.

The transition from level two to level three, i.e., from a random hopping of individual defects to a non-random correlated motion of interacting ions, is found to be accompanied by prominent changes in the shapes of functions which are experimentally accessible. For instance, the ionic conductivity assumes a characteristic frequency dependence, and spin-lattice relaxation rates are no longer properly described by the model of Bloembergen, Purcell and Pound [1] (cf. Chaps. 9 and 20). Surprisingly, the experimental phenomena are very much the same in structurally disordered crystals such as $RbAg_4I_5$, in glasses, and even in supercooled melts.

level two,
random hopping:

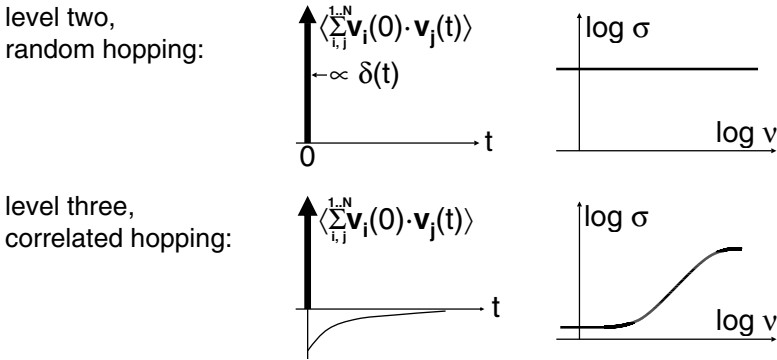level three,
correlated hopping:



**Fig. 21.1.** Random versus correlated jump diffusion.

In this chapter, the diffusive motion of mobile ions in disordered materials will be analysed on the basis of the frequency-dependent electrical (ionic) conductivity, $\sigma(\nu)$. Figure 21.1 illustrates the change observed in the shape of this function as random hopping is replaced by correlated hopping. In Fig. 21.1, we have used a relationship from linear response theory which states that $\hat{\sigma}(\nu)$ is proportional to the Fourier transform of the autocorrelation function of the current density [2]. If all mobile ions have the same charge, the current density will be proportional to the sum of their velocities. Therefore, $\sigma(\nu)$ is proportional to the Fourier transform of the velocity correlation function, $\langle \sum_{i,j}^{1..N} \boldsymbol{v}_i(0) \cdot \boldsymbol{v}_j(t) \rangle$.

If the ions (or mobile defects) are random walkers, as in level two, they do not know of each other, and all the cross terms vanish. Also, random walkers have no memory. Hence each hop is only correlated to itself. On a time scale that does not resolve a few picoseconds, the velocity correlation function is, therefore, proportional to a delta function at time zero, $\delta(t)$. The Fourier transform of a delta function being a constant, $\sigma(\nu)$ will be constant at least up to microwave frequencies. Such a behaviour is indeed observed in the case of level-two materials such as AgBr. By contrast, ionic materials with disordered structures display frequency-dependent conductivities, $\sigma(\nu)$, as in Fig. 21.2. In this case, the conductivity caused by the hopping motion of the ions is well described by a constant minus a bell-shaped contribution centred at $\nu = 0$. The corresponding velocity correlation function is, therefore, characterised by a sharp peak at $t = 0$, plus a decaying negative contribution at $t > 0$, see Fig. 21.1. While the sharp peak once again reflects the self-correlation of the velocity during hops, the decaying negative contribution results from a decaying probability for an ensuing *backward* hop, if the hop performed at time $t = 0$ defines the *forward* direction. If the dc conductivity, $\sigma_{\mathrm{dc}} = \sigma(0)$, is much smaller than the conductivity measured at microwave frequencies, correlated forward-backward hops have to be considered the rule rather than the exception.
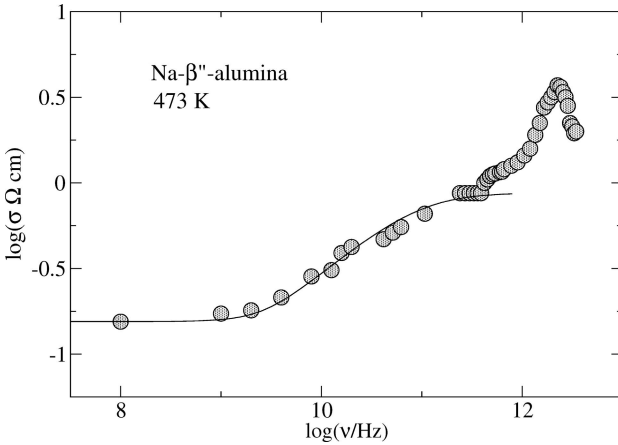
**Fig. 21.2.** Frequency-dependent conductivity, $\sigma(\nu)$, of crystalline Na-$\beta''$-alumina at 473 K [3]. Below 100 GHz, $\sigma(\nu)$ is essentially caused by the hopping motion of the sodium ions, while above 1 THz it is essentially due to the excitation of transverse optical phonons.

There is a direct analogy between this effect and the Debye-Hückel-Onsager-Falkenhagen effect, cf. Fig. 21.3. In Fig. 21.3 (a), consider a dilute strong liquid electrolyte. Suppose an ion is virtually displaced at time zero. As a consequence, it is no longer at the centre of its ion cloud. Two competing relaxation processes tend to restore equilibrium. The ion may move backward or the cloud may move forward. This results in a flow of charge in the direction opposite to the initial displacement, and Fourier transformation of the current density autocorrelation function yields a small increase of the conductivity as a function of frequency.

In a structurally disordered solid electrolyte, see Fig. 21.3 (b), the translational motion is achieved by hops, and the neighbouring mobile ions play the role of the ion cloud. Again, there is a competition between two relaxation processes. After each hop of a mobile ion, the ion may either hop backwards or its neighbours may rearrange. However, there is a striking difference between Fig. 21.3 (a) and Fig. 21.3 (b) concerning the respective magnitude of the effect. The amount of backward flow of charge and hence the resulting dispersion of $\sigma(\nu)$ are dramatically larger in the solid than in the dilute liquid electrolyte.

In this chapter, the correlated ionic motion in materials with disordered structures is studied on the basis of experimental conductivity spectra, $\sigma(\nu)$. In particular, a simple set of rules is derived that grasp the essential aspects of the ion dynamics and outline their development with time. Indeed, experimental conductivity spectra have led us to derive two coupled rate equations which describe the ion dynamics in a very general fashion and provide a means not only for reproducing the frequency-dependent conductivities, but
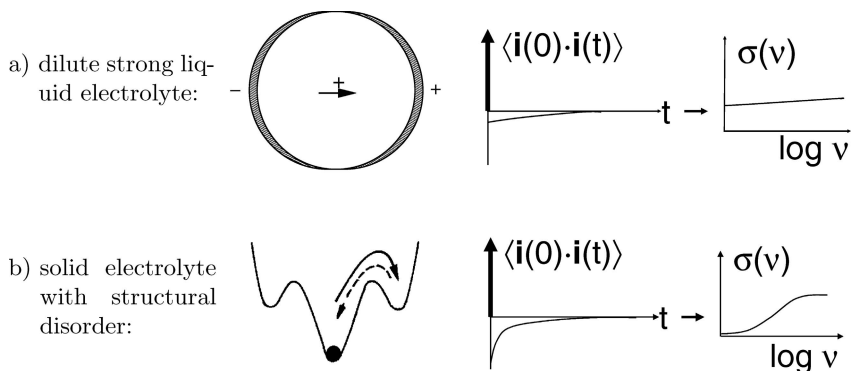
a) dilute strong liquid electrolyte:

b) solid electrolyte with structural disorder:



**Fig. 21.3.** Schematic comparison of the current density autocorrelation function and the conductivity dispersion in a) a dilute strong liquid electrolyte and b) a structurally disordered solid electrolyte.

also for tracing the specific traits of the spectra back to their dynamic origins. These rate equations make up the concept of mismatch and relaxation (CMR), to be presented and discussed in this chapter.

This chapter is organised as follows. In Sect. 21.2, the experimental techniques used in conductivity spectroscopy are briefly introduced, and the characteristic features of frequency- and temperature-dependent conductivities, $\sigma(\nu, T)$, are summarised. In Sect. 21.3, we give a brief outline of the formal relationships between conductivities, $\sigma(\nu)$, and time-dependent correlation functions. We also give interpretations of the experimental features and present models for the ion dynamics on a microscopic scale. In Sect. 21.4, we introduce the two rate equations of the CMR and show how time-dependent functions and realistic model conductivity spectra are obtained from them. Section 21.5 is devoted to a brief discussion of the scaling properties of the model spectra. It also provides relationships between model parameters and characteristic frequencies of the conductivity spectra, thus facilitating their interpretation. The physical concept leading to the two rate equations of the CMR is then outlined in Sect. 21.6. Examples of sets of complete conductivity spectra (extending at least up to millimetre-wave frequencies) taken at different temperatures are presented and discussed in Sects. 21.7 and 21.8, for solid electrolytes and for a fragile supercooled ionic melt, respectively. Section 21.9 deals with the shape of frequency-dependent conductivities of many glassy and crystalline materials as measured in the so-called impedance frequency regime, below some 10 MHz. In Sect. 21.10 we discuss localised movements of interacting charged particles and their manifestation in $\sigma(\nu, T)$.

## 21.2 Conductivity Spectra of Ion Conducting Materials

Conductivity spectroscopy spans more than 17 decades on the frequency scale, ranging from less than $10^{-3}$ Hz to more than $10^{14}$ Hz. The width of the time scale thus covered is unsurpassed by any other technique. Besides offering a broad variety of applications in the characterisation of materials, the technique also provides a unique possibility to study the motion of charged particles (ions or polarons) on rather different time scales, even resolving their elementary hopping processes. Therefore, it plays the role of an extremely powerful 'microscope in time'. A schematic survey of the requisite spectroscopies is given in Fig. 21.4. Experimentally, four frequency regimes may be discerned:

  (i)  the impedance regime, below some 10 MHz,
 (ii)  the radio regime, from some 10 MHz to a few GHz,
(iii)  the microwave regime, from a few GHz to about 150 GHz, and
(iv)  the (far-) infrared regime, above 150 GHz.

Electrodes are used only in (i). Guided electromagnetic waves are employed in (ii) and (iii), and free ones in (iv). Coaxial waveguides are practicable up to 18 GHz. At higher microwave frequencies, they are replaced by rectangular waveguide systems. Fourier transform spectroscopy is the method of choice in the (far) infrared. Although a number of different experimental set-ups are required to cover the entire frequency range, the general procedure towards the electrical characterisation of materials is essentially the same in any part of the spectrum. The complex electrical conductivity, $\widehat{\sigma}(\nu)$, is always determined by measurement of amplitudes and phases of quantities related to the field-induced current in the sample. These are voltages and currents, if electrodes are employed [4–6]. If the experimental technique is electrode-free, the relevant quantities are, instead, complex field amplitudes of electromagnetic waves transmitted or reflected by the sample [7]. In the latter case, the complex conductivity, $\widehat{\sigma}(\nu)$, is obtained from the measured data by means
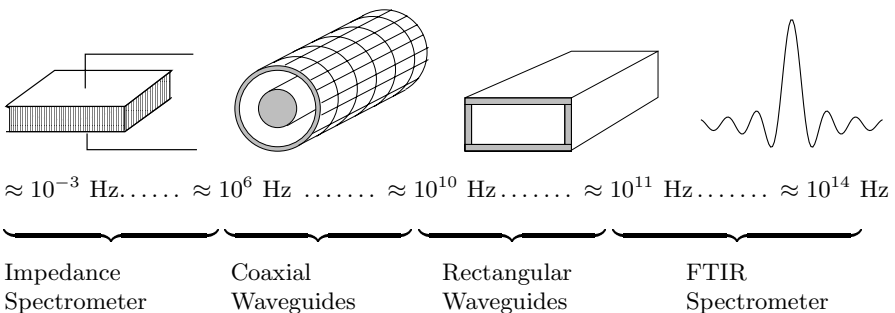


$\approx 10^{-3}$ Hz......  $\approx 10^{6}$ Hz .......  $\approx 10^{10}$ Hz.......  $\approx 10^{11}$ Hz.......  $\approx 10^{14}$ Hz

| Impedance Spectrometer | Coaxial Waveguides | Rectangular Waveguides | FTIR Spectrometer |

**Fig. 21.4.** Schematic overview of different techniques for the measurement of frequency-dependent conductivities.
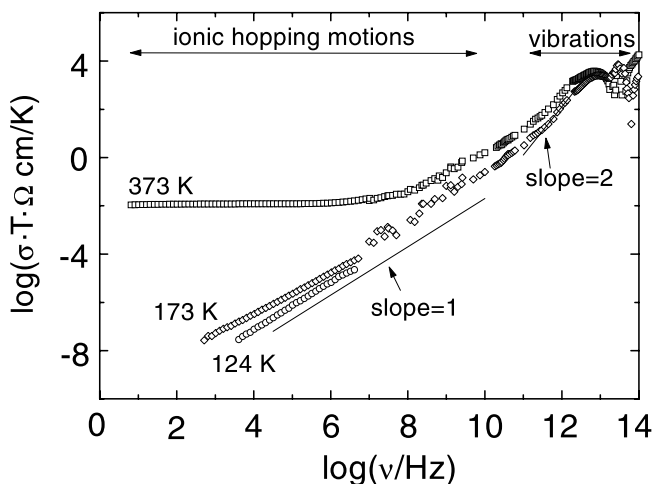
**Fig. 21.5.** Typical conductivity spectra of an ion conducting material, viz., glassy $B_2O_3 \cdot 0.56\,Li_2O \cdot 0.45\,LiBr$.

of Maxwell's equations and the boundary conditions at the interfaces, which guarantee the continuity of the electric and magnetic field components.

In spite of their potential for unravelling microscopic mechanisms of ionic motion, complete conductivity spectra of ion conducting materials, like the one presented in Fig. 21.2, are still very rare. In Fig. 21.5, we present another example, viz., conductivity spectra of glassy $B_2O_3 \cdot 0.56\,Li_2O \cdot 0.45\,LiBr$, extending up to 100 THz. Above 100 GHz, the conductivity is governed by vibrational contributions featuring a $\nu^2$ frequency dependence on the low-frequency flank. In amorphous materials without lattice periodicity there are no selection rules for far-infrared absorption; hence the vibrational peaks are much broader than in crystals, cf. Fig. 21.2.

Conductivity spectra of different ion conducting materials with disordered structures show many common features. Phenomenologically, the following characteristics have been identified:

(i) A dc conductivity plateau, $\sigma_{dc} = \sigma(0)$, is attained at sufficiently low frequencies. In ionic solids and strong ionic melts, $\sigma_{dc} \cdot T$ is usually Arrhenius activated, viz., $\sigma_{dc} \cdot T = A \cdot \exp(-E_{dc}/(k_B T))$, while fragile melts show a pronounced deviation from the Arrhenius law [8].

(ii) The ac conductivity, $\sigma(\nu)$, increases monotonically with frequency [9], at least up to millimetre-wave frequencies. In the very far infrared, displacive and vibrational contributions to $\sigma(\nu)$ are usually hard to distinguish.

(iii) In some cases, however, this distinction has been possible, and the so-called high-frequency plateau, $\sigma_{hf} = \sigma(\infty)$, has been identified. An

example has been given in Fig. 21.2. Wherever detected, high-frequency plateau conductivities are found to obey the Arrhenius law with an activation energy lower than $E_{dc}$ [3,7,10–12].

(iv) Typically, the shape of $\sigma(\nu)$, as observed in a log-log plot below the microwave regime, does not depend on temperature. Therefore, a master curve is obtained when these sections of the conductivity spectra are shifted and superimposed. This is the time-temperature superposition principle [13–17].

(v) In a log-log plot of $\sigma \cdot T$ versus frequency, the onset of the dispersion is often found to occur along a straight line with a slope of one, implying that the onset frequency and $\sigma_{dc} \cdot T$ are both activated with $E_{dc}$. This is the so-called Summerfield scaling [18], exemplified in Fig. 21.6 where conductivity spectra of glassy $0.3\,Na_2O \cdot 0.7\,B_2O_3$ taken at different temperatures have been scaled to fall on a single master curve.

(vi) Master curves constructed from spectra $\sigma(\nu)$ of a large number of different ionic materials with disordered structures are surprisingly similar in shape [15,17,19].

(vii) At any temperature, the initial part of $\sigma(\nu)$ *roughly* follows the Jonscher power law, i.e., $\sigma(\nu) - \sigma(0) \propto \nu^p$ with an exponent $p$ between 0.6 and 0.7 in most cases. This behaviour, found in a broad variety of materials, is often called universal dynamic response (UDR) [20].

(viii) Two-dimensional ion conductors such as the beta aluminas [21], crystals and glasses with low number densities of mobile ions, see Sect. 21.9 and [17], and mixed cation glasses [22,23] exhibit a particularly gradual onset of the dispersion of $\sigma(\nu)$.

(ix) As temperature is decreased, the slope of $\sigma(\nu)$ in the log-log plot approaches the value of one at any given audio or radio frequency, while the conductivity becomes decreasingly temperature-dependent, cf. Fig. 21.5. As $\sigma(\nu) \propto \nu$ corresponds to a frequency-independent dielectric loss, this feature has come to be known as nearly constant loss (NCL) behaviour [24–26].

(x) As a consequence of (vii) and (ix), the typical shape of empirically constructed master curves of ionically conducting materials is characterised by an apparent exponent which increases with increasing reduced frequency, gradually approaching the value of one.

(xi) Remarkably, the NCL feature has also been found in ionic crystals and glasses at cryogenic temperatures, where it is certainly not related to ionic transport [27].
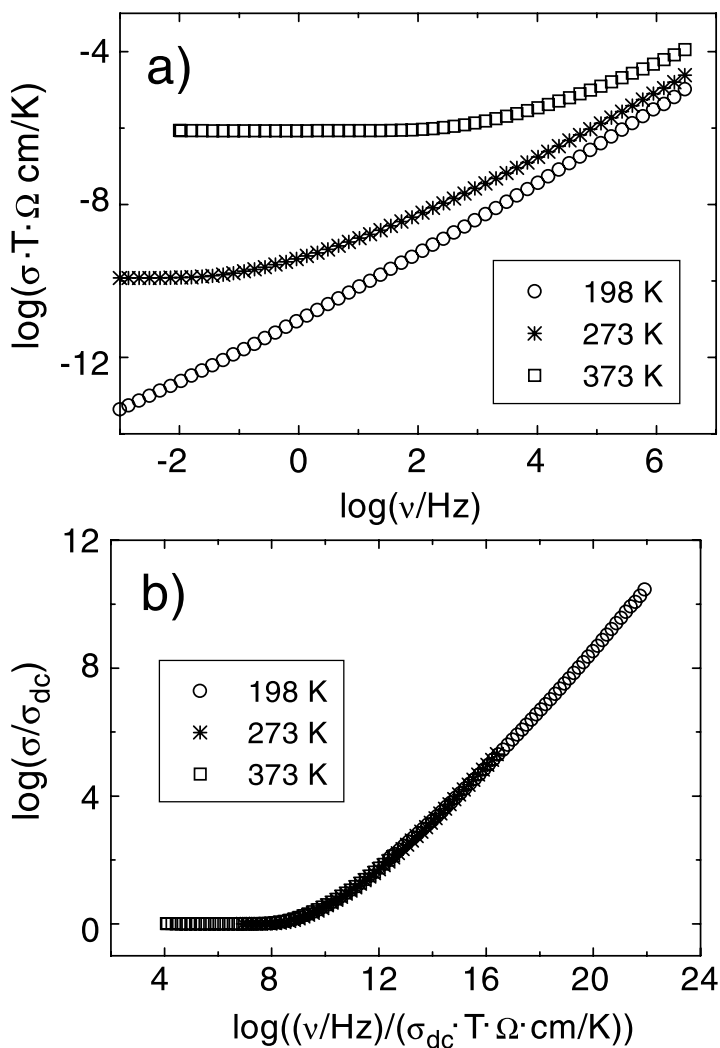
**Fig. 21.6.** a) Experimental conductivity spectra of glassy $0.3\,\mathrm{Na_2O \cdot 0.7\,B_2O_3}$. b) Scaled representation of the data presented in a).

## 21.3 Relevant Functions and Some Model Concepts for Ion Transport in Disordered Systems

Conductivity spectra convey information on the microscopic dynamics of the mobile charge carriers, since according to linear response theory [2], $\widehat{\sigma}(\omega)$, with $\omega = 2\pi\nu$, is the Fourier transform of the autocorrelation function of the current density:

$$\widehat{\sigma}(\omega) = \frac{V}{3k_{\mathrm{B}}T} \cdot \int_0^\infty \langle \boldsymbol{i}(0) \cdot \boldsymbol{i}(t) \rangle \exp(-\mathrm{i}\omega t) \mathrm{d}t \ . \tag{21.1}$$

In (21.1), the current density,

$$\boldsymbol{i}(t) = \frac{1}{V} \sum_{i=1}^N q_i \boldsymbol{v}_i(t) \ , \tag{21.2}$$

and its autocorrelation function are real functions of time. $V$ is the volume of the sample, and the summation is over all $N$ charge carriers. Their charges and velocities are denoted by $q_i$ and $\boldsymbol{v}_i$, respectively. In systems with only one type of mobile charge carrier, the complex conductivity, $\widehat{\sigma}(\omega)$, is connected with the complex coefficient of self diffusion of this carrier, $\widehat{D}(\omega)$, via

$$\widehat{\sigma}(\omega) = \frac{Nq^2}{Vk_{\mathrm{B}}T} \cdot \frac{1}{\widehat{H}_{\mathrm{R}}(\omega)} \cdot \widehat{D}(\omega) \ . \tag{21.3}$$

In (21.3), $\widehat{H}_{\mathrm{R}}(\omega)$ denotes the frequency-dependent complex Haven ratio,

$$\widehat{H}_{\mathrm{R}}(\omega) = \frac{N \int_0^\infty \langle \boldsymbol{v}(0) \cdot \boldsymbol{v}(t) \rangle \, \exp(-\mathrm{i}\omega t) \, \mathrm{d}t}{\int_0^\infty \langle \sum_{i,j}^{1..N} \boldsymbol{v}_i(0) \cdot \boldsymbol{v}_j(t) \rangle \, \exp(-\mathrm{i}\omega t) \, \mathrm{d}t} \ , \tag{21.4}$$

which becomes a real number in its low-frequency limit: $H_{\mathrm{R}} = \widehat{H}_{\mathrm{R}}(\omega = 0)$. If cross correlations between movements of different ions $i, j$ may be neglected, the Haven ratio becomes unity. Within this approximation we then obtain the Nernst-Einstein relation,

$$\widehat{\sigma}(\omega) = \frac{Nq^2}{Vk_{\mathrm{B}}T} \cdot \widehat{D}(\omega) \ . \tag{21.5}$$

Monte-Carlo simulations by Maass et al. [28] have shown that the overall shape of conductivity spectra is indeed well described, if only correlations between hops of a single ion are taken into account. Within this "single particle approximation", the dynamic conductivity can be expressed by the Fourier transform of the velocity autocorrelation function,

$$\widehat{\sigma}(\omega) = \frac{Nq^2}{3Vk_{\mathrm{B}}T} \cdot \int_0^\infty \langle \boldsymbol{v}(0) \cdot \boldsymbol{v}(t) \rangle \exp(-\mathrm{i}\omega t) \, \mathrm{d}t \tag{21.6}$$

$$= -\omega^2 \frac{Nq^2}{6Vk_{\mathrm{B}}T} \cdot \lim_{\epsilon \to 0} \int_0^\infty \langle r^2(t) \rangle \exp(-\epsilon t - \mathrm{i}\omega t) \, \mathrm{d}t \ .$$

Here, $\langle r^2(t) \rangle$ is the time-dependent mean square displacement of the mobile ions. Equation (21.6) implies that the dynamic conductivity can be derived from a model-based velocity autocorrelation function, $\langle \boldsymbol{v}(0) \cdot \boldsymbol{v}(t) \rangle$.

In the most simple approach, the ions are assumed to be random walkers, cf. Fig. 21.1, and the velocity autocorrelation function reads:

$$\langle \boldsymbol{v}(0) \cdot \boldsymbol{v}(t) \rangle_{\text{RW}} = \frac{\Gamma x_0^2}{2} \cdot \delta(t) \ . \tag{21.7}$$

Here $\Gamma$ and $x_0$ are the hopping rate and the elementary jump distance of the ions, respectively. Combination of (21.6) and (21.7) yields a hopping conductivity which is real and constant up to about $100\,\text{GHz}$:

$$\widehat{\sigma}_{\text{RW}} = \sigma_{\text{RW}} = \frac{Nq^2x_0^2\Gamma}{6Vk_{\text{B}}T} \ , \tag{21.8}$$

see also Fig. 21.1.

However, (21.8) is in marked contrast to experimental conductivity spectra like those presented in Figs. 21.2 and 21.5. As outlined in Sect. 21.1, correlated hopping processes of the ions have to be taken into account. In the latter case, both the current density autocorrelation function, $\langle \boldsymbol{i}(0) \cdot \boldsymbol{i}(t) \rangle$, and the velocity autocorrelation function, $\langle \boldsymbol{v}(0) \cdot \boldsymbol{v}(t) \rangle$, strongly deviate from those of a random walker, cf. Fig. 21.1.

Over the years, various concepts, models and computer simulations have been published, all of them aiming at a realistic description of the nonrandom ion transport in disordered systems. The most important ones are briefly summarised in the following.

(i) In his coupling concept, Ngai described the time-dependent decay of an electric field in an electrolyte by joining together an exponential and a stretched-exponential (Kohlrausch-Williams-Watts) decay function. The model yields $\sigma_{\text{dc}} = \sigma(0)$, $\sigma_{\text{hf}} = \sigma(\infty)$, and a dispersive conductivity in between [29–31].

(ii) The physical picture of mismatch and mismatch relaxation was first introduced in the jump relaxation model. Being based on interactions between the ions, the model was able to reproduce essential features of the spectra in a closed expression [32, 33].

(iii) Introducing disorder on a square lattice, Bunde and co-workers obtained time-correlation functions and spectra $\sigma(\nu)$ from Monte-Carlo simulations [34] (see Chap. 20).

(iv) In their counter-ion model, Dieterich and co-workers considered both disorder and interactions and were thus able to derive realistic spectra from numerical simulations [35, 36] (see Chap. 20).

(v) It has been realised that the combined validity of the time-temperature superposition principle and the Summerfield scaling implies that the only effect of temperature is to change the hopping rates of the ions while their hopping mechanism is preserved.

(vi) The asymmetric double well potential (ADWP) model [37] has been used by Nowick, Jain, and their co-workers to explain the NCL behaviour. Jain coined the phrase "jellyfish" behaviour [38]. Both Nowick and Jain have always regarded UDR and NCL as different features [26].

(vii) On the other hand, concepts have also been developed which self-consistently explain a continuous transition from UDR to NCL. One of these is the random barrier model as treated mathematically by Dyre and Schrøder [39, 40]. However, the comparatively large rms value of the distance at which an ion loses memory of its previous position is an unsolved problem of this approach.

(viii) The concept of mismatch and relaxation (CMR) also provides realistic spectra including the UDR-NCL transition. It has the further advantage of reproducing spectra with different shapes in a one-parameter treatment, see the following section.

(ix) On the basis of the CMR, the non-Arrhenius dc conductivity encountered in fragile supercooled ionic melts has been shown to be a direct consequence of a short-time behaviour characterised by Arrhenius-activated elementary displacements normally followed by roll-back processes [12].

(x) According to recent computer simulations [41], the NCL behaviour observed at cryogenic temperatures can be explained by strictly localised movements of interacting ions (cf. Chap. 20). The same result is obtained from a suitably modified version of the CMR [42].

## 21.4 CMR Equations and Model Conductivity Spectra

Before embarking on the construction of the CMR, it is useful to consider the shapes of some relevant functions. This is done with the help of Fig. 21.7, where the approximation of (21.6) has been adopted, i.e., it is assumed that no essential error is introduced by putting $H_R = 1$, cf. [43]. For convenience, one further function is introduced, viz., the time-dependent correlation factor, $W(t)$ [32]. This function is a normalised integral of $\langle \boldsymbol{v}(0) \cdot \boldsymbol{v}(t) \rangle$ and, at the same time, a normalised derivative of the mean square displacement, $\langle r^2(t) \rangle$:

$$\frac{2}{\Gamma_0 x_0^2} \int_0^t \langle \boldsymbol{v}(0) \cdot \boldsymbol{v}(t') \rangle \mathrm{d}t' = W(t) = \frac{1}{\Gamma_0 x_0^2} \frac{\mathrm{d}}{\mathrm{d}t} \langle r^2(t) \rangle \; . \qquad (21.9)$$

Here, $\Gamma_0$ denotes the elementary hopping rate of the ions.

At very short times, when each ion performs at most one hop, correlations are not yet visible. Therefore, we have $W(0) = 1$, and $\langle r^2(t) \rangle$ increases linearly with time, see Fig. 21.7 (b) and Fig. 21.7 (d). Note that the ballistic short-time behaviour, with $\langle r^2(t) \rangle \propto t^2$, is not included as jump processes are considered only. At longer times, when negative values of $\langle \boldsymbol{v}(0) \cdot \boldsymbol{v}(t) \rangle$ contribute significantly to the expression in (21.9), $W(t)$ is found to decay with time, and $\langle r^2(t) \rangle$ increases in a sublinear fashion. This time regime is sometimes called "subdiffusive" or "anomalous" (cf. Chaps. 10, 18, 19, 22).
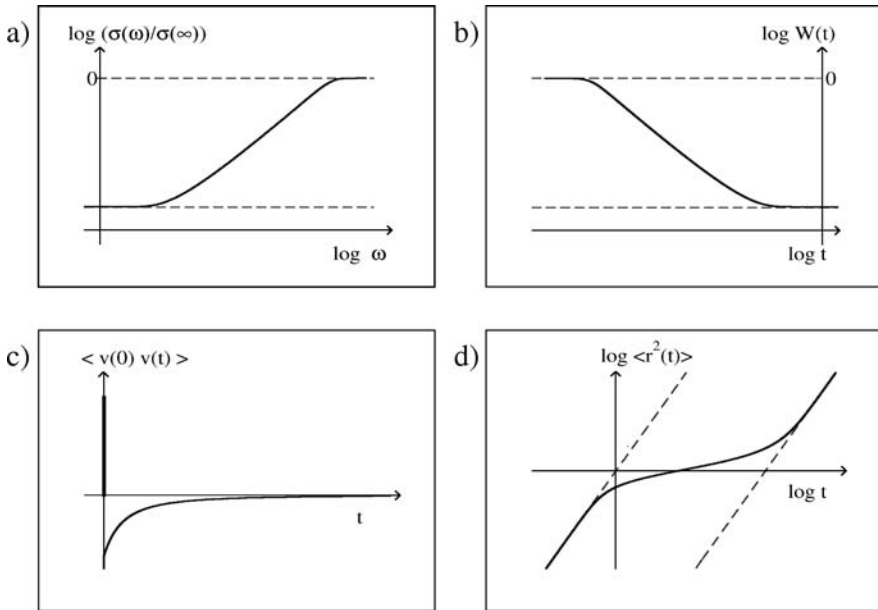
**Fig. 21.7.** Schematic plot of relevant functions. (a) Normalised frequency-dependent conductivity caused by the hopping motion of the ions, versus angular frequency in a log-log representation. (b) Time-dependent correlation factor versus time in a log-log representation. (c) Velocity autocorrelation function of the mobile ions versus time. (d) Mean square displacement of the mobile ions versus time in a log-log representation.

Only at much longer times, when $\langle \boldsymbol{v}(0)\boldsymbol{v}(t) \rangle$ becomes very small and, consequently, $W(t)$ tends to its long-time limit, $W(\infty)$, does $\langle r^2(t) \rangle$ change from its subdiffusive behaviour into its diffusive long-time behaviour, which is linear in time, with $\langle r^2(t) \rangle = 6Dt$, where $D$ is the coefficient of self-diffusion. Note that $\sigma(\nu)/\sigma(\infty)$ and $W(t)$, in log-log representations, are almost perfect mirror images of each other, see Fig. 21.7 (a) and Fig. 21.7 (b) as well as Fig. 21.8. Although this approximate symmetry is useful for practical purposes, we will not use it for deriving model spectra, $\sigma(\nu)/\sigma(\infty)$. Rather, exploiting the relationships between $\sigma(\nu)$ and $\langle \boldsymbol{v}(0)\boldsymbol{v}(t) \rangle$, and between $\langle \boldsymbol{v}(0)\boldsymbol{v}(t) \rangle$ and $W(t)$, we write

$$\frac{\sigma(\nu)}{\sigma(\infty)} = 1 + \int_0^\infty \dot{W}(t) \cos(2\pi\nu t)\mathrm{d}t \ . \tag{21.10}$$

From (21.10) it is evident that $\sigma(\nu)/\sigma(\infty)$ will be known as soon as $W(t)$ is known. The basic idea of the CMR is now to find $W(t)$ from simple rate equations that describe the development of the ion dynamics with time.

In the following, we present the equations that allow us to determine functions $W(t)$ and $\sigma(\nu)/\sigma(\infty)$. We also present and discuss general features of

the conductivity spectra thus obtained, while the explanation of the physical concept of the model is postponed to Sect. 21.6.

The rate equations used in the CMR are

$$-\dot{g}(t) = A\, g^K(t)\, W(t) \tag{21.11}$$

and

$$-\dot{W}(t) = -B\, W(t)\, \dot{g}(t) \,. \tag{21.12}$$

These equations contain two time-dependent functions, $W(t)$ and $g(t)$. Here $W(t)$ is the time-dependent correlation factor, while $g(t)$ is a normalised mismatch function, see Sect. 21.6. They also contain three parameters, viz., $A$, $B$ and $K$. The first parameter, $A$, is an internal frequency which turns out to be proportional to the high-frequency conductivity, $\sigma(\infty)$. The second parameter, $B$, determines the ratio $\sigma(0)/\sigma(\infty) = W(\infty)$ via $W(\infty) = \exp(-B)$. In many cases, $W(\infty)$ is found to be Arrhenius activated which implies that $B$ should be proportional to the inverse temperature, $1/T$. In the following section, see (21.25), we will show that the ratio $A/B$ is not only proportional to $\sigma(\infty) \cdot T$, and hence to the elementary hopping rate of the mobile ions, $\Gamma_0$, but that $A/B$ and $\Gamma_0$ may even be assumed to be identical (at least for the example studied, within the limits of experimental error). The value of the third parameter, $K$, influences the shape of the resulting conductivity spectra in the vicinity of the onset of the dispersion, see the end of this section as well as the discussion at the end of Sect. 21.6. In glassy and crystalline electrolytes with high concentrations of mobile ions, $K$ is typically found to be 2 or close to 2.

Functions $W(t)$ and $g(t)$ satisfying the rate equations are shown in Fig. 21.8 (a). The particular parameter values used are $W(\infty) = 0.001$ and $K = 2$. The time axis has been normalised by multiplication with the internal frequency $A$. In a second step, application of (21.10) yields the normalised conductivity spectrum, $\sigma(\nu)/\sigma(\infty)$, represented in Fig. 21.8 (b) by the solid line. Note that the broken line in Fig. 21.8 (b), obtained from $W(t)$ by forming the mirror image, provides a good approximation to the exact solution, i.e.,

$$\frac{\sigma(\omega)}{\sigma(\infty)} \approx W\left(\frac{2}{\pi\omega}\right) \,. \tag{21.13}$$

Here, the factor $2/\pi$ arises as (21.13) is an approximation for an expression obtained by Fourier transformation. Figure 21.9 shows the shape of the frequency-dependent conductivity for a fixed value of $B$ ($B = 25$), and also demonstrates the effect of varying the parameter $K$. In the first place, it is important to note that, irrespective of the value of $K$, the model conductivity spectra do not obey a power law. Rather, as in Fig. 21.6, the apparent slope in the log-log representation increases continuously, approaching the value of one before the high-frequency plateau is attained. This is the UDR–NCL transition. Of course, this transition can only be observed, if
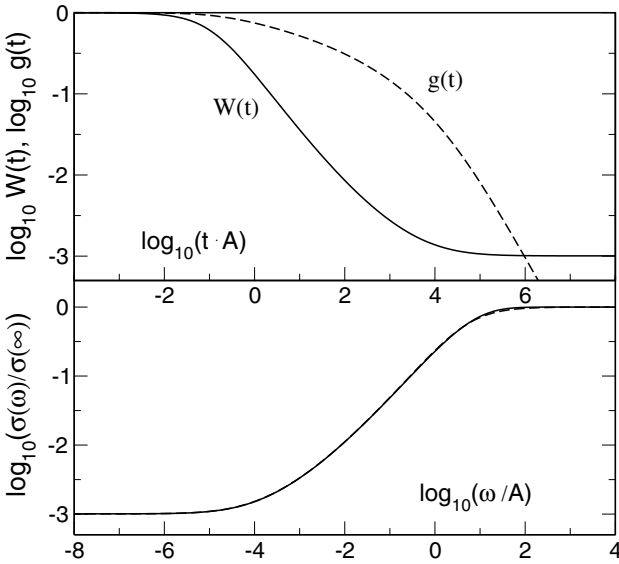
**Fig. 21.8.** (a) Functions $W(t)$ and $g(t)$ satisfying (21.11) and (21.12) for $W(\infty) = \exp(-B) = 0.001$ and $K = 2$. (b) Solid line: normalised conductivity caused by hopping motion versus normalised angular frequency as obtained by inserting $W(t)$ from panel (a) into (21.10). Broken line: mirror-image approximation for the normalised conductivity.
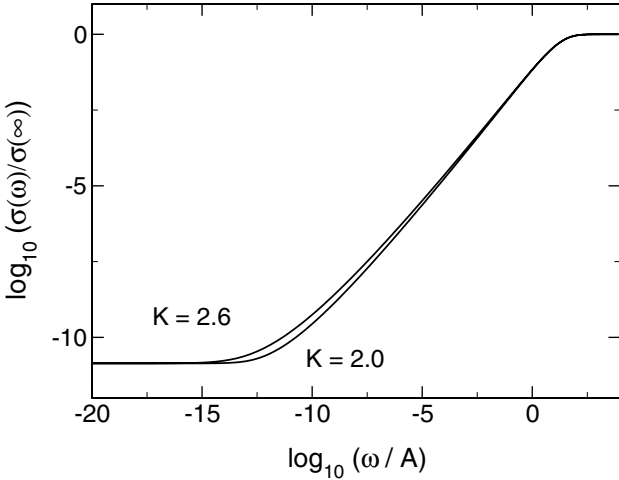


**Fig. 21.9.** Shape of frequency-dependent conductivity as obtained from the CMR for fixed $B$, with $B = 25$, including the effect of different values of $K$.

$W(\infty) = \sigma(0)/\sigma(\infty) = \exp(-B)$ is sufficiently small, i.e., at sufficiently low temperatures. Otherwise, the high-frequency plateau will be attained before the transition becomes visible.

Figure 21.9 also shows how the numerical value of $K$ influences the shape of the spectrum. As $K$ is increased, the transition from $\sigma_{dc} = \sigma(0)$ into the dispersive regime becomes more and more gradual. Indeed, such a variation has been observed experimentally, e.g., upon reducing the number density of mobile ions in a solid electrolyte [17] or when moving from a binary alkali-ion conducting glass into the mixed-alkali regime [22, 23]. Examples will be given in Sect. 21.9.

## 21.5 Scaling Properties of Model Conductivity Spectra

On the basis of (21.11) and (21.12) specific predictions can be made with regard to the behaviour of $W(t)$ and $\sigma(\omega)/\sigma(\infty)$ in the vicinity of those times and angular frequencies that mark the transitions from $\sigma_{dc}$ into the dispersive regime and from the dispersive regime into $\sigma_{hf}$. We will in particular show that model conductivity spectra possess the property of scaling in both limiting cases. This means that the shapes of frequency-dependent model conductivities are preserved in either frequency regime as the temperature is varied. Of course, this requires sufficiently large ratios of $\sigma(\infty)/\sigma(0)$ as well as a fixed value of the parameter $K$.

For the purpose of scaling, temperature-dependent angular frequencies $\omega_O$ and $\omega_E$ will be introduced which mark the onset and the end of the dispersion, respectively.

The situation is particularly simple at short times, when $g(t)$ is still close to one, cf. Fig. 21.8 (a). In this case, (21.11) and (21.12) may be combined and approximated by

$$-\dot{W}(t) = ABW^2(t) . \tag{21.14}$$

Equation (21.14) has the solution

$$W(t) = \frac{1}{1 + ABt} . \tag{21.15}$$

This implies that, according to the mirror image approach, the high-frequency solution for the conductivity should be close to

$$\frac{\sigma(\omega)}{\sigma(\infty)} = \frac{1}{1 + 2AB/(\pi\omega)} . \tag{21.16}$$

We may, therefore, somewhat arbitrarily, define an "end angular frequency" as

$$\omega_E = AB . \tag{21.17}$$

Equation (21.16) is remarkable as it describes the nearly-constant-loss behaviour encountered at angular frequencies $\omega$ below $\omega_E$, provided $g(1/\omega)$ is
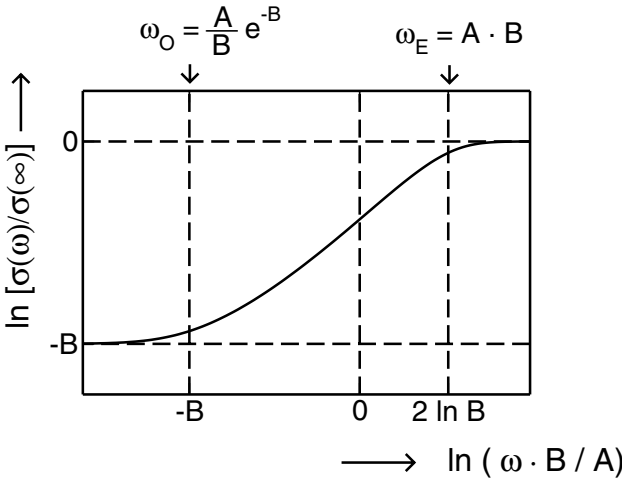
**Fig. 21.10.** A CMR model conductivity spectrum, with $B = 8$ and $K = 2$. The angular frequencies $\omega_O$ and $\omega_E$ mark the onset and the end of the dispersion.

still close to one. At sufficiently low temperatures, this requirement is indeed satisfied in a wide range of angular frequencies that are still well below $\omega_E$. In Fig. 21.10, the position of $\omega_E$ has been marked in a plot of $\ln(\sigma(\omega)/\sigma(\infty))$ versus $\ln(\omega B/A)$. The plot also contains a mark for the corresponding "onset angular frequency", $\omega_O$. An expression for $\omega_O$ is obtained by considering low frequencies, corresponding to long times, where $W_{\mathrm{scaled}} = W(t)/W(\infty)$ tends to unity. In this case we combine (21.11) and (21.12) to form

$$-\frac{\mathrm{d}}{\mathrm{d}t} \ln W_{\mathrm{scaled}}(t) = AB \exp(-B) W_{\mathrm{scaled}}(t) \left[\frac{\ln W_{\mathrm{scaled}}(t)}{B}\right]^K \tag{21.18}$$

or, with

$$\omega_O = AB^{1-K} \exp(-B) \tag{21.19}$$

and

$$t_{\mathrm{scaled}} = t\omega_O , \tag{21.20}$$

$$-\frac{\mathrm{d}}{\mathrm{d}t_{\mathrm{scaled}}} \ln W_{\mathrm{scaled}} = W_{\mathrm{scaled}} \cdot (\ln W_{\mathrm{scaled}})^K . \tag{21.21}$$

Integration of (21.21) yields

$$t_{\mathrm{scaled}} = \int_{\ln W_{\mathrm{scaled}}}^{-\ln W(\infty)} x^{-K} e^{-x} \, \mathrm{d}x \approx \int_{\ln W_{\mathrm{scaled}}}^{\infty} x^{-K} e^{-x} \, \mathrm{d}x . \tag{21.22}$$

The approximation made on the right-hand side of (21.22) is always valid at times that are much longer than $1/\omega_E$. In particular, it is always valid in

the "long-time regime" that corresponds to the impedance frequency range, below 10 MHz. This is important, because experimental conductivities used for scaling purposes have almost exclusively been measured below 10 MHz.

From (21.22) it is evident that in the long-time regime $W_{\mathrm{scaled}}$ is a unique decaying function of $t_{\mathrm{scaled}}$. Correspondingly, $\sigma(\omega)/\sigma(\infty)$ also exhibits scaling, and the "onset angular frequency" may be chosen to be $\omega_{\mathrm{O}}$ from (21.19). In the frequent case of $K = 2$, we have

$$\omega_{\mathrm{O}} = \frac{A}{B} \exp(-B) \quad \text{for } K = 2 . \tag{21.23}$$

This "onset angular frequency" $\omega_{\mathrm{O}}$ has been marked in Fig. 21.10.

The inverse onset angular frequency, $1/\omega_{\mathrm{O}}$ , plays the role of a crossover time at which macroscopic random diffusion is attained. Likewise, a crossover distance, $\ell_{\mathrm{O}}$, may be defined by $\ell_{\mathrm{O}} = (6D/\omega_{\mathrm{O}})^{1/2}$. The example of $RbAg_4I_5$ is particularly clear-cut. In this solid electrolyte, the density of mobile ions is high, the value of $K$ is found to be 2 as in Fig. 21.10, and the elementary hopping distance, $x_0$, is known. From the conductivity spectra of $RbAg_4I_5$, to be discussed in Sect. 21.7, we find that within experimental error there is no difference between $x_0$ and the distance $\ell_{\mathrm{O}}$, after which random diffusion prevails. This means that an ion, after a hop from one site to another, loses its memory of the previous site as soon as it succeeds in stabilising its position at the new one. Therefore, within experimental error, $\omega_{\mathrm{O}}$ can be identified with the "random hopping rate" or "rate of successful hops" of the ions, $\Gamma$:

$$\omega_{\mathrm{O}} \approx \Gamma = 6D/x_0^2 . \tag{21.24}$$

Equation (21.24) is expected to hold not only in the particular case of $RbAg_4I_5$ but in many other ionic materials as well.

As only a fraction $\Gamma/\Gamma_0 = W(\infty) = \exp(-B)$ of all hops are successful, we find that the elementary hopping rate should be

$$\Gamma_0 = \Gamma \cdot \exp(B) \approx \omega_{\mathrm{O}} \exp(B) = \frac{A}{B} \quad \text{for } K = 2 . \tag{21.25}$$

As illustrated in Fig. 21.10, the position of $A/B \approx \Gamma_0$ is situated between $\omega_{\mathrm{O}} \approx \Gamma$ and $\omega_{\mathrm{E}} = AB$ on the frequency scale.

In most crystalline and glassy electrolytes, the dc conductivity, $\sigma_{\mathrm{dc}} = \sigma(\infty) \exp(-B)$ is found to obey the Arrhenius law. This means that $\sigma_{\mathrm{dc}} \cdot T$ is proportional to $\exp(-E_{\mathrm{dc}}/k_{\mathrm{B}}T)$, where $E_{\mathrm{dc}}$ is the activation energy. In those cases, where high-frequency conductivities, $\sigma(\infty)$, have also been determined, they turn out to be Arrhenius activated as well, cf. Sect. 21.2. Conductivity spectra of this kind are easily reproduced by the CMR, with $A$ and $B$ depending on temperature in a known and simple fashion, and a complete set of isothermal conductivity spectra at different temperatures is readily constructed, as shown in Fig. 21.11. According to (21.24), the onset
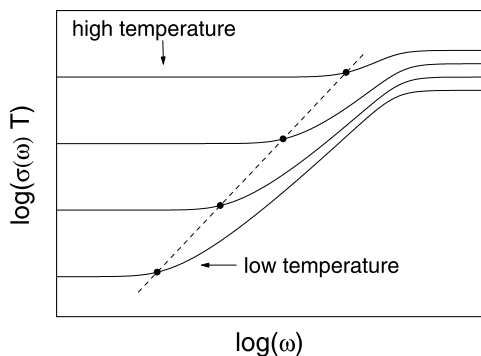
Fig. 21.11. Sketch of a set of frequency-dependent conductivity isotherms as obtained from the CMR for the case where dc conductivity and high-frequency conductivity both follow the Arrhenius law. The value of the parameter $K$ is again 2.

angular frequency is expected to be proportional to the coefficient of self-diffusion and, because of the Nernst-Einstein relation, also proportional to the product of dc conductivity and temperature. In Fig. 21.11, the onset of the dispersion at different temperatures is, therefore, marked by a straight line with a slope of one. This kind of scaling, with $\omega_O \propto \sigma(0) \cdot T$, is sometimes called "Summerfield scaling" [18] and has already been mentioned in Sect. 21.2.

Figure 21.11 also shows that shifting individual conductivity spectra along the line with slope one will result in a superposition of their low-frequency sections. This procedure was applied in Fig. 21.6, producing one experimental master curve and, likewise, one model master curve. The same procedure has proved successful for many glassy and crystalline electrolytes. Further examples are glassy $B_2O_3 \cdot 0.56\,Li_2O \cdot 0.45\,LiBr$, cf. Fig. 21.12, and glassy $0.3\,Li_2O \cdot 0.7\,B_2O_3$, cf. Fig. 21.18 in Sect. 21.9.

Experimentally, materials usually do not display noticeable variations in the shapes of their low-frequency conductivities as the temperature is changed. In the CMR, this corresponds to a fixed value of the parameter $K$. Recently, changes in shape have, however, been observed in the temperature-dependent conductivity spectra of the mixed alkali glass $0.3\,[x\,Li_2O \cdot (1 - x)\,Na_2O] \cdot 0.7\,B_2O_3$ [23].

## 21.6 Physical Concept of the CMR

The concept of mismatch and relaxation builds on the jump relaxation model [32, 33], the central idea being unchanged. Each mobile ion is assumed to have vacant sites in its immediate neighbourhood, while other mobile ions are present in its further surroundings, very much like the ion cloud in Debye-Hückel theory. Due to their mutual repulsive interaction, the ions tend to stay at some distance from each other. Each ion experiences a time-dependent effective potential which consists in part of the static potential provided by the immobile crystalline or glassy network and in part of a time-dependent
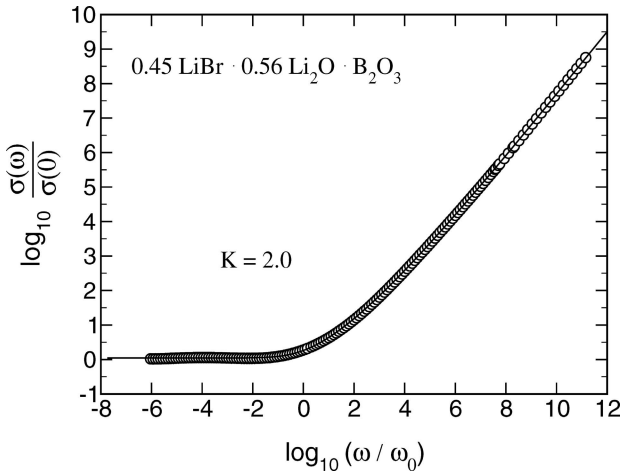
**Fig. 21.12.** Scaled representation of experimental and model conductivities (circles and solid line, respectively) for $B_2O_3 \cdot 0.56\,Li_2O \cdot 0.45\,LiBr$ glass. The value of $K$ is again 2. For more details on this particular system, see [23].

cage-effect potential provided by its mobile neighbours. Suppose the ion performs a hop to a neighbouring site. As a consequence, mismatch will usually be created between its own position and the momentary arrangement of its mobile neighbours. There are two possible ways for the system to reduce the mismatch. Either the neighbours rearrange or the "central" ion hops back into its previous site. This explains the existence of forward-backward correlations of successive hops. Consequently, the mean square displacement exhibits a "subdiffusive" behaviour, cf. Fig. 21.7 (d), and dispersion is observed in frequency-dependent ionic conductivities.

Suppose mismatch is created by a hop of a mobile ion at time $t = 0$. Then the mismatch function $g(t)$, for $t > 0$, has the meaning of a normalised distance between the actual position of the ion and the position at which it would be optimally relaxed with respect to the momentary arrangement of its mobile neighbours. The function $g(t)$ varies with time from $g(0) = 1$ to $g(\infty) = 0$, describing the way mismatch decays because the neighbouring ions rearrange, while the "central" ion is supposed to stay at its position. The negative time derivative, $-\dot{g}(t)$, is thus the rate of mismatch relaxation on the "many-particle route". On the other hand, $-\dot{W}(t)/W(t)$ is interpreted as the rate of mismatch relaxation on the "single-particle route", with the ion hopping backwards. Here, the factor $1/W(t)$ is required, since we focus on those cases where the ion has not yet moved backwards at time $t$. The central assumption of the CMR is then expressed by (21.12), i.e., the rates of relaxation on the single- and many-particle routes are assumed to be proportional to each other at all times. In other words, the tendency for the central

ion to hop backwards is assumed to be proportional to the tendency of its neighbours to rearrange.

Up to this point, the CMR and its predecessor, the jump relaxation model, are identical. The CMR differs from the jump relaxation model by inclusion of (21.11). In this equation, we consider the rate of decay of $g(t)$, $-\dot{g}(t)$. Here it is important to realise that $g(t)$ plays the role of a normalised dipole moment. Its dipole field is the driving force felt by the neighbouring mobile ions, inducing their rearrangement and, as a consequence, the concomitant decay of $g(t)$ itself. As the rearrangement of the surrounding "ion cloud" proceeds, the central dipole will become increasingly shielded. This means that two effects occur simultaneously. One is the decay of $g(t)$ with time. The other is the shrinking of the effective volume of the dipole field. In other words, the effective number of mobile neighbours available for the relaxation becomes time-dependent. It is evident that this is an extremely complicated dynamic process, much more complicated than Debye-Hückel theory. Any attempt to grasp its essence in a simple equation must contain approximations. For deriving a suitable equation we start from the relation,

$$-\dot{g}(t) \propto g(t) * \langle \boldsymbol{v}(0)\boldsymbol{v}(t) \rangle \cdot \#(t) . \tag{21.26}$$

Here, the rate of decay of $g(t)$ at time $t$ is expected to be proportional to the convolution, denoted by "$*$", of the driving force and the velocity auto-correlation function of the neighbouring mobile ions. No distinction is made between the velocity autocorrelation function of the central ion and that of its mobile neighbours. Furthermore, the rate of decay of $g(t)$ is expected to be also proportional to a function $\#(t)$ denoting the time-dependent effective number of mobile neighbours available for the relaxation.

It is now easy to show numerically that $g(t)$ varies with time much more slowly than $\langle \boldsymbol{v}(0)\boldsymbol{v}(t) \rangle$ does. As a consequence, the convolution is well approximated by the product of $g(t)$ and the time integral of $\langle \boldsymbol{v}(0)\boldsymbol{v}(t) \rangle$, which is proportional to $W(t)$. Indeed, functions $g(t)$ and $W(t)$ obtained by use of the approximation are found to satisfy the exact equation (with the convolution) perfectly [12]. Equation (21.26) thus becomes

$$-\dot{g}(t) \propto g(t)\, W(t) \cdot \#(t) . \tag{21.27}$$

While $\#(t)$ is certainly a decaying function of time, its shape is not easily determined from simple model considerations. Therefore, in a more empirical approach, we have tried to determine its shape by comparing experimental spectra, $\sigma(\nu)$, and model spectra obtained from (21.10), (21.12), and (21.27) using functions $\#(t)$ with different shapes. As a result, good agreement between model spectra and experimental spectra is obtained, if $\#(t)$ is assumed to decay as $g(t)$ or slightly faster. This results in (21.11) with $K = 2$ or $K > 2$.

Interestingly, the value of $K$ appears to be related to the overall number density of mobile ions. If the number density is high, then $K \approx 2$ gives

excellent results in most cases, implying that $\#(t)$ should be roughly proportional to $g(t)$. Smaller number densities are reflected by a more gradual increase of $\sigma(\nu)$ in the vicinity of the onset angular frequency, $\omega_O$. According to Fig. 21.9, this corresponds to a larger value of $K$ implying a more rapid decay of $\#(t)$, cf. (21.27). A tentative simple explanation of this effect may be as follows. Let us assume the unshielded effective volume of the dipole field and the number of mobile ions contained in it do, indeed, decay with time in the same fashion as $g(t)$ does. Then, if the overall number density of mobile ions is large, the difference between the number of mobile ions contained in that volume and the number $\#(t)$ will not be significant, since it is only one (the "central" ion). However, if the number density becomes smaller, then this difference becomes increasingly significant. The function $\#(t)$ will then decay faster than $g(t)$, and the effect will be the more pronounced, the smaller the number density is.

At this point, we should like to compare the model concept of the CMR with approaches that focus on the effects of static disordered energy landscapes on the ion dynamics, see e.g. [39, 44]. In either treatment, each mobile ion encounters varying potentials in the course of time. In a static energy landscape, this happens as the ion explores larger and larger parts of its neighbourhood. In the CMR, however, this happens locally, as the potential is considered time-dependent itself. Therefore, the characteristic length $\ell_O$ after which a mobile ion loses memory of a previous site and starts to diffuse at random will necessarily be larger in models with static energy landscapes than it is in the CMR. Here it is important to note that, in agreement with the CMR approach, we find $\ell_O = x_0$ from the data available for rubidium silver iodide, see Sects. 21.5 and 21.7.

## 21.7 Complete Conductivity Spectra of Solid Ion Conductors

The vast majority of measurements of frequency-dependent conductivities of solid ion conductors have been performed in the impedance frequency regime, below 10 MHz. There are only few examples where measurements have been extended into the radio, microwave and far-infrared frequency ranges. Of course, measurement of such "complete" conductivity spectra is a prerequisite for detecting the high-frequency plateau. Nevertheless, the detection of the high-frequency plateau often poses severe experimental problems, in particular in the case of glassy electrolytes, where it is usually swamped by the vibrational contributions to the conductivity, cf. Sect. 21.2 and [45]. In a few cases, however, the variation of the vibrational far-infrared conductivity with frequency is so clear-cut that attempts to remove it appear justified. An example is the glassy electrolyte silver thio germanate, of composition $0.5 \, Ag_2S \cdot 0.5 \, GeS_2$, where conductivity spectra have been taken continuously up to infrared frequencies [46]. In this case it has been possible to prove that,
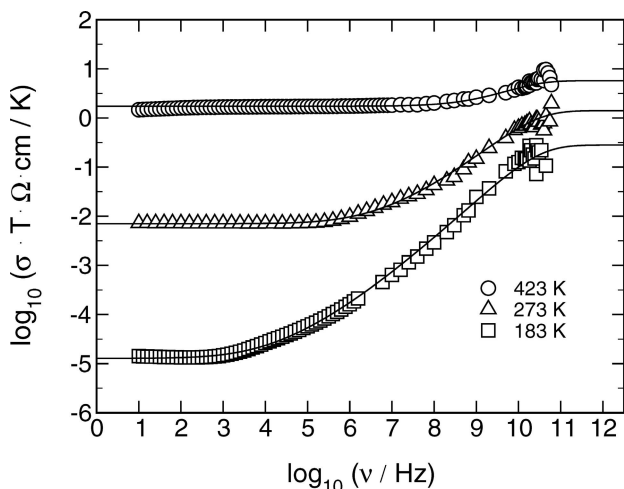
**Fig. 21.13.** Conductivity spectra of $0.5\,Ag_2S \cdot 0.5\,GeS_2$ glass, after removal of vibrational contributions. The solid lines result from the CMR. As in Fig. 21.11, the values of $A(T)$ and $B(T)$ have been chosen such that both dc and hf conductivity are Arrhenius activated. The value of $K$ is 2.3.

within the limits of error, the low-frequency flank of the vibrational conductivity is exactly proportional to frequency squared [23]. In Fig. 21.13 we show a set of non-vibrational conductivity spectra of glassy $0.5\,Ag_2S \cdot 0.5\,GeS_2$ which have been obtained from the original ones by removing the vibrational component. Although the uncertainty introduced by this procedure is considerable at microwave frequencies above $10\,GHz$, it is evident that the spectra of Fig. 21.13 closely resemble the model spectra of Fig. 21.11. The solid lines included in Fig. 21.13 are CMR model spectra. Both $A/B$ and $\exp(-B)$ are thermally activated, the activation energies of $A/B$ and $\sigma(\infty) \cdot T$ being identical. The best choice for the value of $K$ is 2.3.

While the spectra of Fig. 21.13 suffer from the scatter of the data in the microwave regime, the separation of the vibrational and non-vibrational contributions to $\sigma(\nu)$ is less problematic in the case of crystalline rubidium silver iodide, $RbAg_4I_5$, see Fig. 21.14.

$RbAg_4I_5$ is a prominent member of the class of optimised silver ion conductors with structurally disordered silver sublattices [47–49]. High-frequency conductivity spectra of $RbAg_4I_5$ extending up to infrared frequencies have been published in [7,10,50]. In the microwave regime and below, the conductivity is dominated by the translational motion of the silver ions via tetrahedral sites. Slow vibrations of the silver ions within their flat potentials have been shown to be responsible for a maximum in $\sigma(\nu)$ observed in the far infrared, at about $0.5\,THz$ [50]. Conductivity maxima beyond $1\,THz$ are due
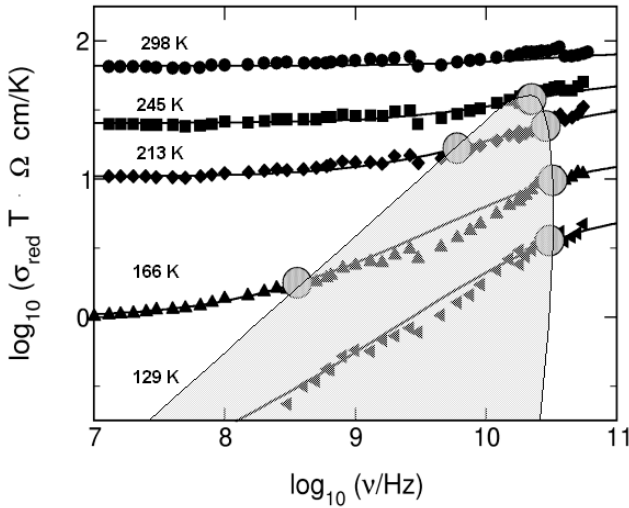
**Fig. 21.14.** Radio and microwave conductivities of the crystalline fast ion conductor RbAg$_4$I$_5$ at different temperatures. The notation $\sigma_{\mathrm{red}}$ indicates that vibrational contributions to the conductivity have been removed. The solid lines result from the CMR, with $K = 2$, the shaded area marks the dispersive regime. For details, see text.

to the excitation of transverse optical phonons (cf. Fig. 21.2 for the case of Na-$\beta''$-alumina).

The non-vibrational radio and microwave conductivity isotherms of Fig. 21.14 have been obtained from the experimental spectra by removing the low-frequency flank of the slow vibrational contribution. At millimetre-wave frequencies, they gradually approach their high-frequency plateaux. Again, the product $\sigma(\infty) \cdot T$ is thermally activated, the activation energy now being $E_{\mathrm{hf}} = 0.053\,\mathrm{eV} \pm 0.005\,\mathrm{eV}$. As noted earlier, this value is identical with the potential barrier between adjacent tetrahedral sites in RbAg$_4$I$_5$ as derived from a probability density contour map for the silver ions [50]. This identity is not surprising, since elementary hops are registered individually in the high-frequency limit.

In Fig. 21.14, CMR model spectra are presented along with the experimental ones. The values of the parameter $A$ are found to be exactly proportional to $\sigma(\infty)$, while the best choice for $K$ is 2.0. For each dispersive spectrum, the onset of the frequency dependence is marked in the figure at $\nu_{\mathrm{O}} = \omega_{\mathrm{O}}/(2\pi)$, while its end is marked at $\nu_{\mathrm{E}} = \omega_{\mathrm{E}}/(2\pi)$. In Fig. 21.14, the onset frequencies $\nu_{\mathrm{O}}$ lie on a straight line with a slope of one, signifying the validity of the Summerfield scaling on the low-frequency side of the dispersion. As noted earlier, the values of $\omega_{\mathrm{O}}(T) = (A(T)/B(T)) \exp(-B(T))$ and those of the random hopping rate, $\Gamma(T)$, of the mobile silver ions are found to be identical within the experimental limits of error:

$$\omega_O(T) \approx \Gamma(T) \,. \tag{21.28}$$

To determine $\Gamma(T)$, we have used the Nernst-Einstein relation,

$$\Gamma(T) \approx \frac{6\sigma(0)k_B T}{N_V e^2 x_0^2} \,, \tag{21.29}$$

where $N_V$ and $e$ denote the number density of the silver ions and the elementary charge, respectively. The Haven ratio has not been included in (21.29) as it is close to one [43]. As a consequence of (21.28), the ratio $A(T)/B(T)$ has to be interpreted as the elementary hopping rate, $\Gamma_0(T)$, cf. Sect. 21.5. Equation (21.28) also implies that the time when random diffusion is attained corresponds to a root mean square displacement of about one elementary hopping distance.

In Fig. 21.14, the marks for $\nu_O$ and $\nu_E$ are on the edge of a shaded area. Within this area the spectra display dispersion, while they become flat outside. On the frequency scale, the width of the shaded area is found to shrink as the temperature is increased, until a particular point is attained at its top, resembling a critical point and signifying the end of the dispersive regime. We thus observe, for the first time in a solid ion conductor, a smooth transition from a non-random hopping at lower temperatures to a random hopping at higher temperatures. In fact, at 298 K the "ion cloud" appears to relax almost instantaneously after each hop of the "central ion", leaving no energetic advantage for a correlated backward hop and no memory of the previously occupied site.

For $W(\infty) = \exp(-B)$ we observe a gradual transition from a thermally activated low-temperature behaviour to its high-temperature value of one. Because of the relation $\sigma(0) = \exp(-B) \cdot \sigma(\infty)$, this has the following implication. In an Arrhenius plot of the dc conductivity, there is a slight, gradual change of slope as $\sigma(0)$ approaches $\sigma(\infty)$ with increasing temperature. In fact, this kind of non-Arrhenius behaviour appears to be characteristic of a number of fast ion conductors, both crystalline and glassy. Examples include Na-$\beta''$-alumina [51,52], argyrodite ($Ag_7GeSe_5I$) [53], and glasses of the system $AgI - Ag_2S - B_2S_3 - SiS_2$ [54].

## 21.8 Ion Dynamics in a Fragile Supercooled Melt

Comparing the dynamics of the mobile ions in glassy and crystalline electrolytes on the one hand and in fragile supercooled ionic melts such as $0.6\,KNO_3 \cdot 0.4\,Ca(NO_3)_2$ [11] and $LiCl \cdot 7\,H_2O$ [12] on the other, one finds surprising similarities as well as characteristic differences. Both are outlined in this section. Considering the fragile melt $LiCl \cdot 7\,H_2O$, we show that the CMR is, indeed, applicable to this system [42].

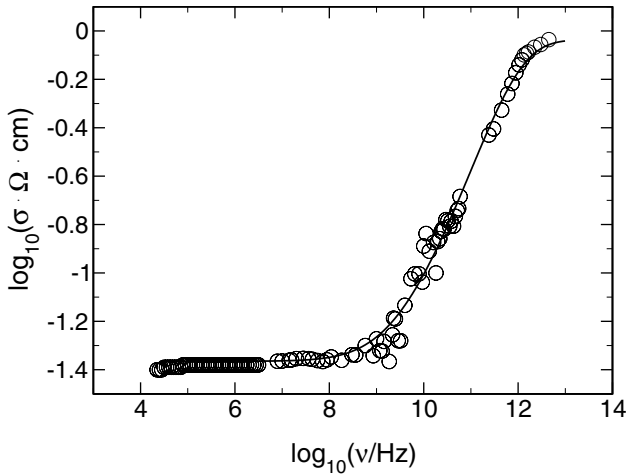**Fig. 21.15.** Non-vibrational conductivity spectrum of the fragile supercooled ionic melt LiCl · 7 H$_2$O at 253 K. The solid line is a CMR model spectrum, with $K = 2$.

In the case of supercooled LiCl · 7 H$_2$O, careful removal of the low-frequency part of the vibrational contribution to the conductivity results in non-vibrational conductivity spectra as the one presented in Fig. 21.15. At frequencies around 1 THz, the spectrum of Fig. 21.15 is seen to level off and to approach its high-frequency plateau. In the figure, a CMR model spectrum is included for comparison. Here, the numerical value of $K$ used for modelling has again been chosen to be 2.0 [42]. The same value of $K$ has also been used for fitting four other $\sigma(\nu)$ isotherms, and the entire set of CMR model spectra thus obtained is presented in Fig. 21.16. Interestingly, the high-frequency conductivities of Fig. 21.16 turn out to follow the Arrhenius law, with a thermal activation energy of 0.08 eV ± 0.005 eV for $\sigma(\infty) \cdot T$ [12].

The observation of a thermally activated high-frequency conductivity in a melt impacts strongly on the assessment of model approaches for the ion dynamics. Evidently, the melt behaves solid-like, if the time window is not larger than a fraction of a picosecond. In this short-time regime, one may visualise individual activated displacements of individual ions. At longer times, however, the structure does not remain rigid. Structural relaxation sets in, and the concept of fixed sites has to be abandoned. Nevertheless, the CMR equations, (21.11) and (21.12), still seem to apply. Conceptually, it is now important to separate the two routes of relaxation expressed by the two equations. In particular, it is important to note that by definition $-\dot{g}(t)$ is the rate of mismatch relaxation due to the rearrangement of the neighbours under the virtual condition $W(t) \equiv 1$, i.e., without considering the backward motion of the central ion itself. Therefore, the factor $W(t)$ is once again included in (21.12). Also, the meaning of $W(t)$ itself is different from what it
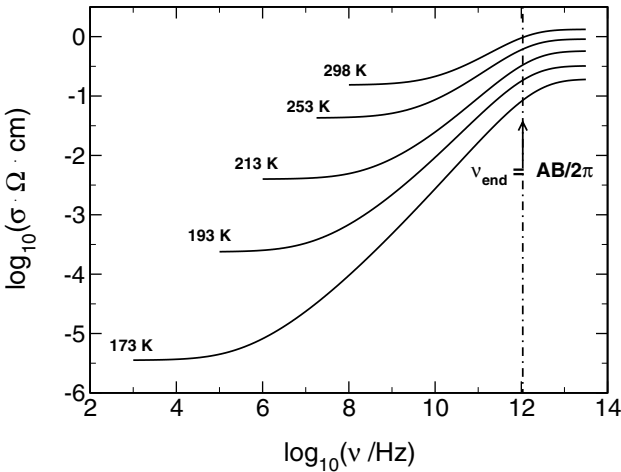
**Fig. 21.16.** Set of CMR model isotherms for the fragile supercooled ionic melt LiCl·
$7\,H_2O$ obtained on the basis of experimental conductivity spectra as in Fig. 21.15,
with $K = 2$.

is in a solid. The function now denotes the average fraction of an original
displacement that is still encountered at time $t$.

It is most interesting to compare the conductivity isotherms of Fig. 21.16
with those of Fig. 21.11. The spectra shown in the two figures have many
properties in common. Firstly, they display the same shape, even the value of
$K$ being identical. Secondly, the high-frequency conductivities are Arrhenius
activated in both cases. Thirdly, the time-temperature superposition princi-
ple appears to be satisfied not only in the solid electrolyte, but also in the
supercooled melt. Nevertheless, the two systems differ strongly with regard
to the temperature dependence of their dc conductivities. In contrast to the
example of Fig. 21.11, the dc conductivity is clearly non-Arrhenius in the case
of the fragile supercooled melt. Most remarkably, this property turns out to
be a direct consequence of the short-time dynamics of the mobile ions.

The key feature causing the non-Arrhenius behaviour of the dc conduc-
tivity is, in fact, the constancy of the crossover angular frequency at the end
of the dispersive regime, $\omega_E = AB$, as a function of temperature, which is
evident from Fig. 21.16. As a consequence of $\omega_E(T) = A(T)B(T) = const.$
and $A(T) \propto \sigma_{hf}(T)$, $B(T)$ is proportional to $1/\sigma_{hf}(T)$. As the dc conductivity
varies with temperature as $\sigma_{dc}(T) = \sigma_{hf}(T)\exp(-B)$, we find

$$\sigma_{dc}(T) = \sigma_{hf}(T) \cdot \exp\left(-\frac{\sigma^*}{\sigma_{hf}(T)}\right) \; , \qquad (21.30)$$

where $\sigma^*$ is a constant. Equation (21.30) replaces the empirical Vogel-Fulcher-
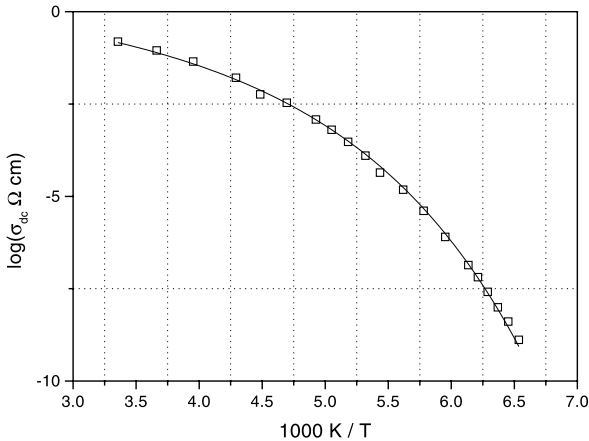Tammann [55–57] relation. Apart from resulting from the short-time dynam-

**Fig. 21.17.** Dc conductivity data of LiCl $\cdot$ 7 H$_2$O. The solid line is from (21.30), see main text.

ics, it has the further advantage of not predicting a singularity of the temperature derivative of the dc conductivity.

The temperature-dependent dc conductivity of LiCl $\cdot$ 7 H$_2$O is plotted in Fig. 21.17. Here, the squares mark our data points [12], while the solid line is obtained from (21.30) with Arrhenius-activated high-frequency conductivities taken from Fig. 21.16. The meaning of the constant $\sigma^*$ becomes obvious by extrapolating (21.30) to a higher temperature $T^*$, where $B$ is only one. For that particular temperature, $\sigma^*$ and $\sigma_{\mathrm{hf}}$ are identical.

Finally, it is worth emphasising that the distinguishing mark of a fragile melt, resulting in (21.30), is the absence of any temperature dependence of the crossover angular frequency $\omega_{\mathrm{E}}$. This feature corresponds to a non-activated roll-back process occurring in most cases after a thermally activated displacement. Such a view of the short-time dynamics is well in line with the conception of a fragile melt as an ionic system whose structure does not easily provide preexisting neighbouring sites for its mobile ions. The situation would be different in a strong glass-forming melt, where (21.30) would not apply, the reason being the existence of available neighbouring sites in the network. The backward hop from such a site would require some activation energy, and hence $\omega_{\mathrm{E}}$ would become temperature-dependent.

## 21.9 Conductivities of Glassy and Crystalline Electrolytes Below 10 MHz

Below 10 MHz, where waveguide techniques are not required, conductivities of materials are measured not only much more easily, but also with much higher precision than at higher frequencies. Therefore, characteristic variations in

the shapes of conductivity spectra of solid electrolytes are best detected in the low-frequency range. In this section, low-frequency conductivities of various glassy and crystalline ion conductors are presented and compared with CMR model spectra. The result of the comparison turns out to be twofold. In the first place, we find that the model conductivities always agree very well with the experimental ones. However, to achieve good agreement, different values of the parameter $K$ have to be adopted, and the remaining question is how to relate those values to the structures and dynamics of the materials studied.

In Fig. 21.18, we present frequency-dependent conductivities of a lithium borate glass of composition $0.3\,Li_2O \cdot 0.7\,B_2O_3$ as measured at four different temperatures. The dc values of the conductivities follow the Arrhenius law. The solid lines included in the figure are CMR model spectra calculated with $K = 2.0$. Both the experimental and the model conductivities satisfy the time-temperature superposition principle, and the Summerfield scaling is found to apply. Utilising the Summerfield scaling, the four experimental spectra can be collapsed in one master curve which is, indeed, indistinguishable from those already shown for other glasses in Fig. 21.6 and Fig. 21.12. Likewise, the model spectra are automatically collapsed in one curve, if the angular frequency is scaled in units of $\omega_O = (A/B)\exp(-B)$, as described in Sect. 21.5. The master spectrum thus obtained and the one of Figs. 21.6 and 21.12 are identical, since the value of $K$ is 2.0 in all cases.

More examples of low-frequency conductivity spectra of glassy electrolytes are given in Figs. 21.19 and 21.20. The data have been taken from a silver sulphate silver metaphosphate glass of composition $0.3\,Ag_2SO_4 \cdot 0.7\,AgPO_3$ [42] and from a mixed alkali-alkaline-earth silicate glass of composition $K_2O \cdot$



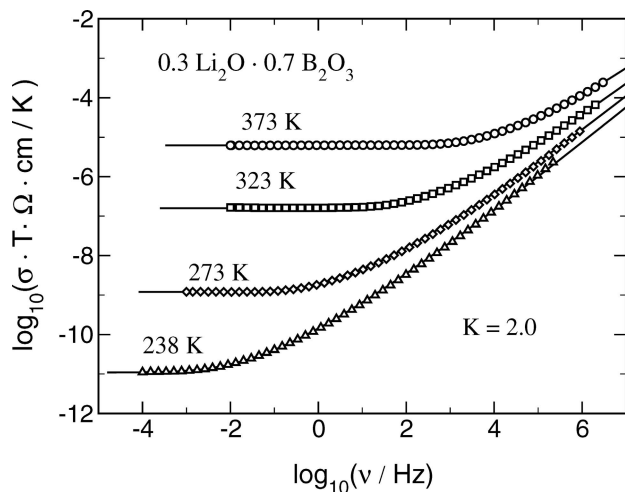**Fig. 21.18.** Comparison of CMR model conductivities (solid lines, $K = 2$) and experimental ones (symbols) for $0.3\,Li_2O \cdot 0.7\,B_2O_3$ glass at different temperatures.
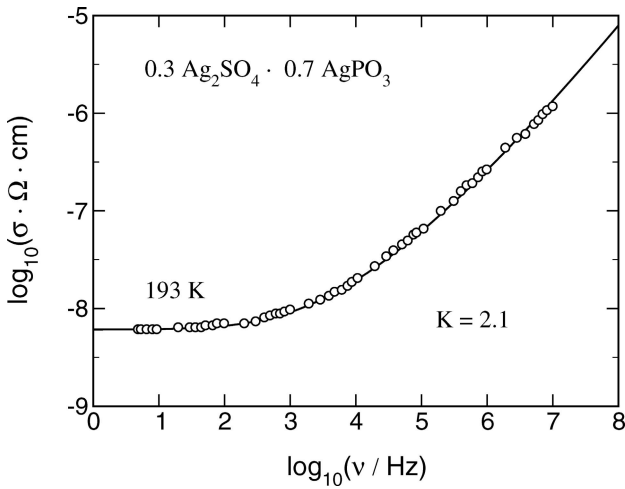
**Fig. 21.19.** Experimental conductivity isotherm of glassy $0.3\,Ag_2SO_4 \cdot 0.7\,AgPO_3$ at $193\,K$ (circles) and CMR model spectrum with $K = 2.1$ (solid line).
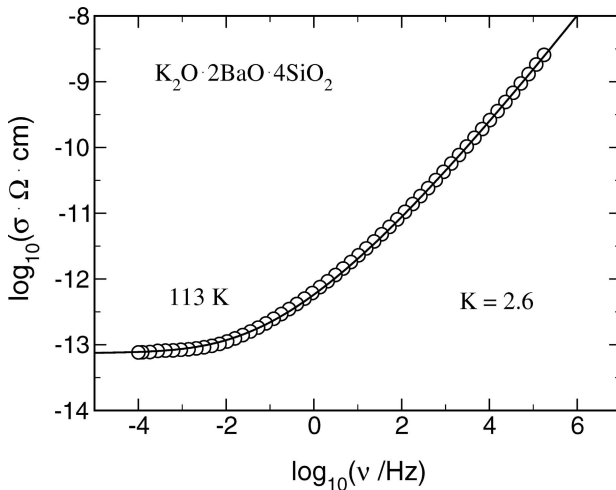


**Fig. 21.20.** Experimental conductivity isotherm of glassy $K_2O \cdot 2\,BaO \cdot 4\,SiO_2$ at $113\,K$ (circles) and CMR model spectrum with $K = 2.6$ (solid line).

$2\,BaO \cdot 4\,SiO_2$ [42], respectively. The data of Fig. 21.19 are best reproduced with $K = 2.1$, while a considerably larger value of $K$, viz., 2.6, is required to describe the frequency-dependent conductivity of the mixed cation glass of Fig. 21.20. The rather gradual onset of the dispersion observed in Fig. 21.20 is reminiscent of many mixed alkali glasses, where the same feature
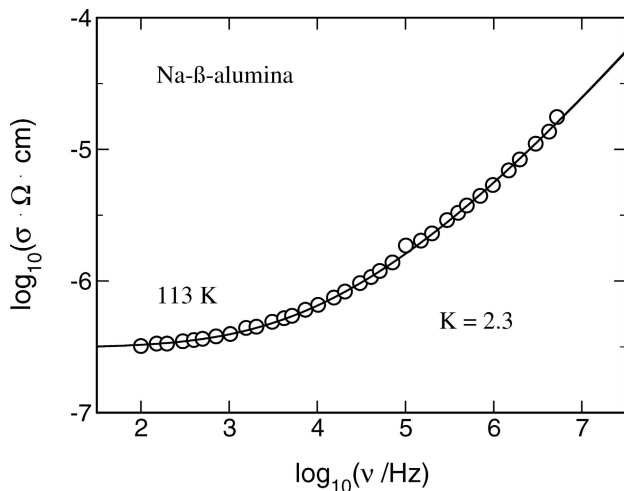
**Fig. 21.21.** Experimental conductivity isotherm of Na-$\beta$-alumina at $113\,\mathrm{K}$ (circles) [58] and CMR model spectrum with $K = 2.3$.

has been identified as a characteristic property of their frequency-dependent conductivities [22].

Values of $K$ larger than 2 are not only found for mixed-cation glasses, but also for crystalline ion conductors with a reduced dimensionality of the sublattice of the mobile ions. The effect of dimensionality on the shape of conductivity spectra has recently been pointed out by Sidebottom [21]. (For the influence of reduced dimensionality on neutron scattering and NMR spin-lattice relaxation results see Chap. 3 and 9, respectively.) The most famous two dimensional fast ion conductor is probably Na-$\beta$-alumina. In Fig. 21.21, we reproduce conductivity data of this material published by Almond, West and Grant [58]. To reproduce the data in terms of the CMR, the best choice of $K$ is 2.3.

Crystalline electrolytes in which the number of mobile ions is limited by the particular defect structure constitute another interesting class of materials. Examples are the low-temperature $\gamma$-phase of $RbAg_4I_5$, stable below the first-order $\beta$-$\gamma$-transition at $122\,\mathrm{K}$ [59] and $\beta$-AgI where the defect structure is frozen-in at reduced temperatures. In both cases, the conductivity spectra are well reproduced by the CMR, if $K$ is chosen to be as high as 2.6 [42,60]. A spectrum of $\beta$-AgI is shown in Fig. 21.22, while the case of $\gamma$-$RbAg_4I_5$ will be discussed in Sect. 21.10.

The impression that $K$ may be causally related to the number density of translationally mobile ionic charge cariers is thus corroborated. The view that enhanced values of $K$ correspond to a reduced number density of potentially mobile ions in the neighbourhood of the "central" ion also seems to agree with the observation that large values of $K$ are found in mixed cation glasses
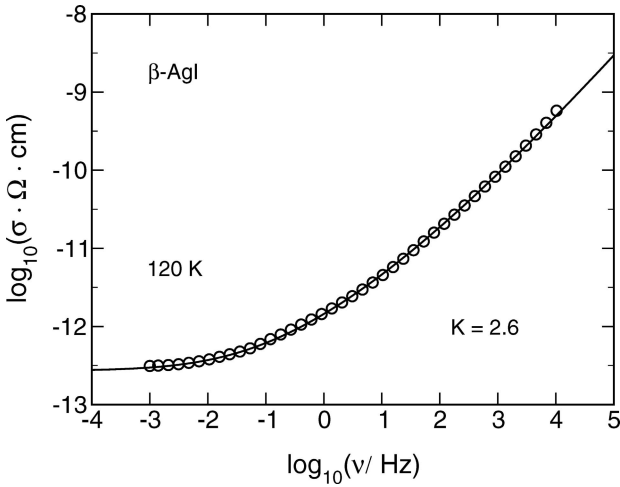
**Fig. 21.22.** Experimental conductivity isotherm of $\beta$-AgI at 120 K (circles) [58] and CMR model spectrum with $K = 2.6$.

as well. In such glasses, only a fraction of the neighbouring ions may be considered mobile, since most of them are unable to find suitable sites in their immediate neighbourhood. In spite of the above pieces of evidence, it is felt that the tentative interpretation towards an understanding of the meaning of $K$ given at the end of Sect. 21.6 is not yet sufficiently conclusive. Rather, further investigations are required to get a better insight into this problem.

## 21.10 Localised Motion at Low Temperatures

The short-time solution for $W(t)$ as given in (21.15) applies as long as $g(t)$ is close to one. This is the case in a broad interval on the logarithmic time scale, if $B$ is sufficiently large. Equation (21.15) then corresponds to a conductivity that increases almost linearly with frequency, before the high-frequency plateau is attained. Approaching this regime from low frequencies, the CMR predicts a continuous increase of the apparent power-law exponent, with one as a limiting value. Experimentally, such a behaviour has been observed in many ion-conducting solid materials, both crystalline and glassy, cf. Fig. 21.5. Another agreement between experimental and model conductivities concerns the very small temperature dependence in the NCL regime. As outlined in Sect. 21.5, the low-frequency parts of spectra like those in Fig. 21.11 can be superimposed by shifting them along a line with a slope of one. This implies that at frequencies where $\sigma(\omega) \propto \omega$ is roughly satisfied, the temperature dependence of the conductivity should, indeed, become very small.
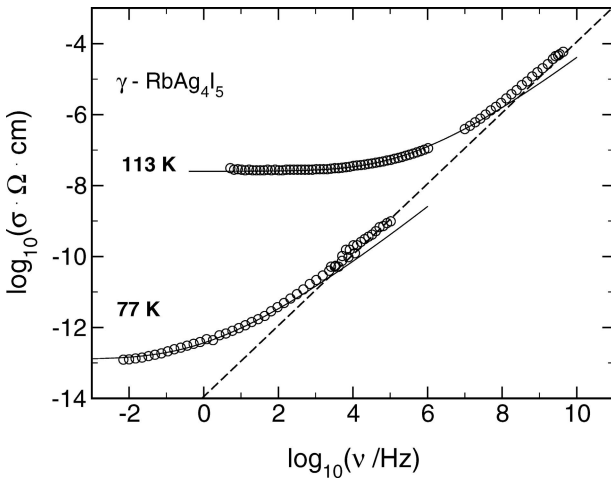
**Fig. 21.23.** Two conductivity isotherms of RbAg$_4$I$_5$ taken in the low-temperature $\gamma$-phase (circles). The solid lines are CMR model spectra, with $K = 2.6$.

Interestingly, an approximately linear dependence $\sigma(\omega) \propto \omega$ has been found in the impedance frequency regime not only in materials featuring non-zero dc conductivities, but also in cases where, at a few Kelvin, ionic hopping transport can be safely excluded as the cause of the effect [26, 27, 61, 62]. To explain such data, one has to envisage small localised displacements over low potential barriers. It appears obvious that in this process interactions between locally mobile ionic charge carriers will play an important role.

The purpose of this section is twofold. In the first place, we show that the CMR equations, when slightly modified, are able to describe completely localised movements of interacting ions, reproducing the low-temperature NCL behaviour. Secondly, we present experimental conductivity spectra featuring the CMR behaviour as outlined in Sects. 21.4 to 21.6 *plus* the low-temperature NCL effect. In fact, in the $\gamma$-phase of rubidium silver iodide, cf. Fig. 21.23, both types of ionic motion appear to contribute simultaneously to the frequency-dependent conductivity. This will be discussed at the end of this section.

In the literature, the low-temperature NCL behaviour is usually described in terms of the asymmetric double well potential (ADWP) model [37]. In that model, the potentials considered are static and exhibit particular distributions of their barrier energies and asymmetries. The resulting conductivity spectra have the same features as the one presented in Fig. 21.24. As the frequency is increased, the slope in the log-log plot of $\sigma(\omega)$ changes first from two to one and later from one to zero. The two crossover angular frequencies correspond to a longest and a shortest relaxation time. However, there are two aspects to the ADWP model that appear unsatisfactory. One is the ne-
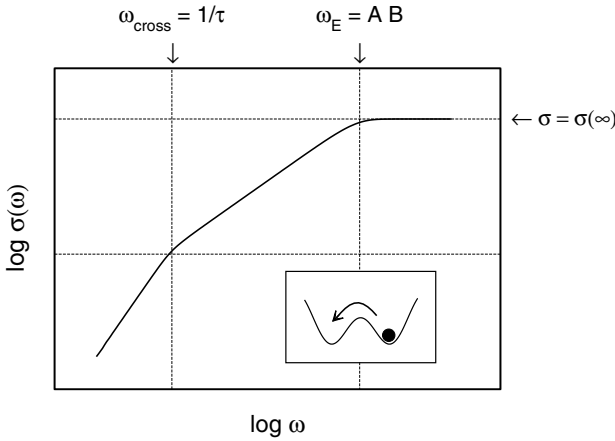
**Fig. 21.24.** CMR model conductivity spectrum for an assembly of interacting localised ions in flat double-well potentials ($B = 100$, $A\tau = 10^6$).

cessity to assume particular distributions. The other is the lack of any time dependence in the shape of the potentials. Of course, such a time dependence has to be expected, reflecting the interactions with other ions which are also locally mobile. Indeed, if the dynamics of local electric dipoles are simulated on a computer, and if interactions between them are taken into account, particular distributions turn out to be unnecessary, and the spectra obtained again display the features of the one shown in Fig. 21.24 [41] (cf. Chap. 20).

The derivation of the conductivity spectrum of Fig. 21.24 has not required any particular distribution, nor a computer simulation. Instead, the CMR has been used to introduce the interaction. The rationale is as follows. Without any interaction, the dynamics of an individual ion in a flat double-well potential would be properly described by an exponentially decaying function $W(t)$. This would imply $-(\mathrm{d}W(t)/\mathrm{d}t)/W(t) = 1/\tau$, where $\tau$ is the relaxation time. Taking interactions with other dipoles into account, we replace the right-hand side with $-B \cdot \mathrm{d}g(t)/\mathrm{d}t + 1/\tau$ and again describe the decay of the normalised mismatch function, $g(t)$, by the short-time version of (21.11):

$$-\frac{\mathrm{d}}{\mathrm{d}t}g(t) = A \cdot g^K(t) \cdot W(t) \simeq A \cdot W(t) \qquad (21.31)$$

$$-\left(\frac{\mathrm{d}}{\mathrm{d}t}W(t)\right) \cdot \frac{1}{W(t)} = -B \cdot \frac{\mathrm{d}}{\mathrm{d}t}g(t) + \frac{1}{\tau} . \qquad (21.32)$$

At low temperatures, $1/\tau$ is only a small additive constant on the right-hand side of (21.32). At short times, when $1/\tau$ is still much smaller than $-B \cdot \mathrm{d}g(t)/\mathrm{d}t$, the functions $W(t)$ and $\sigma(\omega)/\sigma(\infty)$ obtained from (21.31) and (21.32) are almost identical with those obtained without inclusion of $1/\tau$. If the dc conductivity is extremely low, corresponding to a large value

of $B$, and if $1/\tau$ is small, we thus find a nearly-constant-loss behaviour in a wide range of frequencies. At very long times, however, when $-B \cdot \mathrm{d}g(t)/\mathrm{d}t$ becomes even smaller than $1/\tau$, $W(t)$ will decay exponentially. This results in a $\sigma(\omega) \propto \omega^2$ behaviour at low frequencies. Both features are clearly seen in Fig. 21.24.

The crossover from the $\sigma(\omega) \propto \omega^2$ regime into the NCL regime occurs at an angular frequency $\omega_{\mathrm{cross}} = 1/t_{\mathrm{cross}}$. At the particular time $t_{\mathrm{cross}}$, the two terms on the right-hand side of (21.32) become identical. As $g(t)$ is still close to unity, we find from (21.31) and (21.32) that $W(t_{\mathrm{cross}})$ should be $1/(AB\tau)$. On either axis of a $\sigma(\omega)$ plot, the corresponding crossover point and the high-frequency crossover point (at angular frequency $\omega_{\mathrm{E}} = AB$) should, therefore, be apart from each other by a factor of $AB\tau$. This implies

$$\omega_{\mathrm{cross}} = 1/\tau \qquad (21.33)$$

as indicated in Fig. 21.24.

In Fig. 21.23, the CMR model curves provide fits to the experimental conductivities of $\gamma$-RbAg$_4$I$_5$ only at sufficiently low frequencies, while increasing discrepancies are observed at higher frequencies. Forming the difference between the measured conductivity isotherms and the model curves we obtain the same straight line with a slope of one at both temperatures. This extra contribution to the conductivity of $\gamma$-RbAg$_4$I$_5$ is thus – within the limits of experimental error – both linear in $\omega$ and temperature-independent. It is, therefore, interpreted as resulting from a strictly localised ionic motion as described by (21.31) and (21.32). In the $\alpha$- and $\beta$-phases of RbAg$_4$I$_5$ where all the silver ions are translationally mobile, this contribution to $\sigma(\omega)$ has not been detected, as it is evidently swamped by the regular CMR spectrum. For a complete and satisfactory description of the ion dynamics in $\gamma$-RbAg$_4$I$_5$ it will, of course, be important to elucidate the detailed structural properties of this phase, which are still unknown.

The conductivity isotherms of Fig. 21.23 are especially valuable, as they put an end to a long-standing discussion. Until now, there have been two seemingly contradictory points of view. Authors who have been measuring ionic conductivities over wide ranges of frequency and temperature have been convinced that the NCL behaviour is observed in any structurally disordered solid electrolyte, if $\sigma(\nu)/\sigma(0)$ is sufficiently large, but $\sigma_{\mathrm{hf}}$ is not yet attained, the effect being caused by the short-time hopping dynamics of the mobile ions [63, 64]. On the other hand, those who have been measuring nearly constant losses at low temperatures, have been convinced that this effect is certainly not related with ionic hopping and ionic transport [27, 62]. The two views are now reconciled, since Fig. 21.23 provides an example where the strictly localised kind of ionic motion is found to coexist with the translational one.

## 21.11 Conclusion

Conductivity spectra of ionic materials with disordered structures contain valuable information on the diffusion dynamics of the mobile ions. Phenomenologically, they display a number of common features. For any *given* ion conducting material, these include the time-temperature superposition principle and the UDR – NCL transition. With regard to *different* ion conducting materials, they include surprisingly close similarities in the shapes of the spectra of crystalline, glassy, and even molten systems. On the other hand, specific differences are also observed concerning, e.g., the temperature dependence of the dc conductivity and the way $\sigma(\nu)$ increases in the vicinity of the onset frequency of the dispersion.

In this chapter, we have presented a set of simple rules, expressed in the form of rate equations, which describe the development of the ion dynamics with time. The rules reproduce the observed phenomena and explain them in terms of microscopic processes. Our CMR model bears analogy to Debye-Hückel-Falkenhagen theory in considering the coupling between mobile ions and their surrounding ion clouds. It is able to reproduce and explain the time-temperature superposition principle as well as the UDR – NCL transition and the low-temperature NCL behaviour. The specific differences in shape encountered in conductivity spectra of different ion conducting materials are reproduced with the help of only one parameter, $K$. Although it is clear that there is a connection between $K$ and the number density of the mobile ions, more work is required in order to quantify this relationship.

### Notation

| | |
|---|---|
| $A$ | parameter of the CMR model; internal frequency |
| $B$ | parameter of the CMR model: $B = \ln(\sigma(\infty)/\sigma(0))$ |
| $D$ | coefficient of self diffusion |
| $e$ | elementary charge |
| $E_{dc}$ | activation energy of the dc conductivity |
| $g(t)$ | normalised mismatch function, normalised dipole field |
| $H_R$ | Haven ratio |
| $\boldsymbol{i}$ | current density |
| $\langle \boldsymbol{i}(0) \cdot \boldsymbol{i}(t) \rangle$ | current density autocorrelation function |
| i | imaginary unit, $\mathrm{i} = \sqrt{-1}$ |
| $k_B$ | Boltzmann constant |
| $\ell_O$ | characteristic length for loss of memory |
| $N$ | number of mobile carriers |
| $N_V$ | particle density |
| $q$ | electrical charge |
| $\langle r^2(t) \rangle$ | mean square displacement |
| $t$ | time |
| $T$ | temperature |

| | |
|---|---|
| $\boldsymbol{v}$ | velocity |
| $\langle \boldsymbol{v}(0) \cdot \boldsymbol{v}(t) \rangle$ | velocity autocorrelation function |
| $V$ | volume |
| $W(t)$ | time dependent correlation factor |
| $x_0$ | jump distance |
| $\Gamma$ | rate of "successful" hops, random hopping rate |
| $\Gamma_0$ | elementary hopping rate |
| $\nu$ | frequency |
| $\sigma$ | electrical conductivity |
| $\omega$ | angular frequency |
| $\omega_\mathrm{O}$ | angular frequency marking the onset of dispersion |
| $\omega_\mathrm{E}$ | angular frequency marking the end of dispersion |
| $\#(t)$ | effective number of mobile ions available for relaxation |

Complex quantities are marked by a circumflex ("$\widehat{\phantom{x}}$").

# References

1. N. Bloembergen, E.M. Purcell, R.V. Pound: Phys. Rev. **73**, 679 (1948)
2. R. Kubo: J. Phys. Soc. Japan **12**, 570 (1957)
3. C. Cramer, R. Graeber, M.D. Ingram, T. Saatkamp, D. Wilmer, K. Funke: Mat. Res. Soc. Symp. Proc. **369**, 233 (1995)
4. B. A. Boukamp: Solid State Ionics **18/19**, 136 (1986)
5. *Impedance Spectroscopy: Emphasizing Solid State Materials and Systems*, ed by J.R. MacDonald (Wiley, New York 1987)
6. I. Riess: Solid State Ionics **91**, 221 (1996)
7. R. Hoppe, T. Kloidt, K. Funke: Ber. Bunsenges. Phys. Chem. **95**, 1025 (1991)
8. C.A. Angell: J. Non-Cryst. Solids **131-133**, 13 (1991)
9. J.C. Kimball, L.W. Adams Jr: Phys. Rev. B **18**, 5851 (1978)
10. K. Funke, T. Kloidt, D. Wilmer, C.J. Carlile: Solid State Ionics **53-56**, 947 (1992)
11. K. Funke: Z. Phys. Chem. **206**, 101 (1998)
12. K. Funke, B. Heimann, M. Vering, D. Wilmer: J. Electrochem. Soc. **A148**, 395 (2001)
13. H. E. Taylor: Trans. Faraday Soc. **52**, 873 (1956)
14. J.O. Isard: J. Non-Cryst. Solids **4**, 357 (1970)
15. H. Kahnt: Ber. Bunsenges. Phys. Chem. **95**, 1021 (1991)
16. B. Roling, A. Happe, K. Funke, M. Ingram: Phys. Rev. Lett. **78**, 2160 (1997)
17. B. Roling: Solid State Ionics **105**, 185 (1998)
18. S. Summerfield: Phil. Mag. B **52**, 9 (1985)
19. J. C. Dyre: J. Appl. Phys. **64**, 2456 (1988)
20. A. K. Jonscher: Nature **267**, 673 (1977)
21. D. L. Sidebottom: Phys. Rev. Lett. **83**, 983 (1999)
22. B. Roling, C. Martiny: Phys. Rev. Lett. **85**, 1274 (2000)
23. C. Cramer, S. Brückner, Y. Gao, K. Funke: Phys. Chem. Chem. Phys. **4**, 3214 (2002)
24. W.-K. Lee, J.F. Liu, A.S. Nowick: Phys. Rev. Lett. **67**, 1559 (1991)

25. A.S. Nowick, B.S. Lim, A.V. Vaysleyb: J. Non-Cryst. Solids **172-174**, 1243 (1994)
26. H. Jain, S. Krishnaswami: Solid State Ionics **105**, 129 (1998)
27. X. Lu, H. Jain: J. Phys. Chem. Solids **55**, 1433 (1994)
28. P. Maass, J. Petersen, A. Bunde, W. Dieterich, H.E. Roman: Phys. Rev. Lett. **66**, 52 (1991)
29. K. L. Ngai: Comments Solid State Phys. **9**, 127 (1979)
30. K. L. Ngai: Comments Solid State Phys. **9**, 141 (1980)
31. K. L. Ngai: Solid State Ionics **5**, 27 (1981)
32. K. Funke: Prog. Solid St. Chem. **22**, 111 (1993)
33. K. Funke: Solid State Ionics **94**, 27 (1997)
34. P. Maass, M. Meyer, A. Bunde: Phys. Rev. B **51**, 8164 (1995)
35. D. Knödler, P. Pendzig, W. Dieterich: Solid State Ionics **70-71**, 356 (1994)
36. D. Knödler, P. Pendzig, W. Dieterich: Solid State Ionics **86-88**, 29 (1996)
37. M. Pollak, G.E. Pike: Phys. Rev. Lett. **28**, 1449 (1972)
38. H. Jain: Met. Mater. Process. **11**, 317 (1999)
39. J.C. Dyre, T.B. Schrøder: Rev. Mod. Phys. **72**, 873 (2000)
40. J.C. Dyre, T.B. Schrøder: Phys. Rev. Lett. **84**, 310 (2000)
41. B. Rinn, W. Dieterich, P. Maass: Phil. Mag. B **77**, 1283 (1998)
42. K. Funke, R.D. Banhatti, S. Brückner, C. Cramer, C. Krieger, A. Mandanici, C. Martiny, I. Ross: Phys. Chem. Chem. Phys. **4**, 3155 (2002)
43. K. Funke: Prog. Solid St. Chem. **11**, 345 (1976)
44. J.C. Dyre: Phys. Rev. B **49**, 11709 (1994)
45. K. Funke, C. Cramer, B. Roling: Glastechnol. Ber. Glass Sci. Technol. **73**, 244 (2000)
46. R. Belin, G. Taillades, A. Pradel, M. Ribes: Solid State Ionics **136-137**, 1025 (2000)
47. B.B. Owens, G.R. Argue: Science **157**, 308 (1967)
48. S. Geller: Science **157**, 310 (1967)
49. J.N. Bradley, P.D. Greene: Trans. Farad. Soc. **63**, 424 (1967)
50. K. Funke, H.J. Schneider: Solid State Ionics **13**, 335 (1984)
51. W.L. Roth, R.L. Beneson, W.K. Tikku, J.L. Briant, B. Dunn: Solid State Ionics **5**, 163 (1981)
52. J.C. Bates, H. Engstrom, J.C. Wang, B.C. Larson, N.J. Dudney, W.E. Brundage: Solid State Ionics **5**, 159 (1981)
53. A. Zerouale, B. Deroide, B. Cros, M. Ribes: Solid State Ionics **28-30**, 1317 (1988)
54. J. Kincs, S.W. Martin: Phys. Rev. Lett. **76**, 70 (1996)
55. H. Vogel: Phys. Z. **22**, 645 (1921)
56. G.S. Fulcher: J. Am. Ceram. Soc. **8**, 339 (1925)
57. V.G. Tammann, H. Hesse: Z. Anorg. Chem. **156**, 245 (1926)
58. D. Almond, A. West, R. Grant: Solid State Commun. **44**, 1277 (1982)
59. W.V. Johnston, H. Wiedersich, G.W. Lindberg: J. Chem. Phys. **51**, 3739 (1969)
60. K. Funke, R.D. Banhatti, I. Ross, D. Wilmer: Z. Phys. Chem. **217**, 1245 (2003)
61. A.S. Nowick, A.V. Vayleyb, W. Liu: Solid State Ionics **105**, 121 (1998)
62. A.S. Nowick: Solid State Ionics **136-137**, 1307 (2000)
63. B. Roling, C. Martiny, S. Murugavel: Phys. Rev. Lett. **87**, 85901 (2001)
64. K. Funke, B. Roling, M. Lange: Solid State Ionics **105**, 195 (1998)